Progress Report: Subsidence in the Central Valley, California

Tom G Farr, Cathleen Jones, Zhen Liu
Jet Propulsion Laboratory
California Institute of Technology

Executive summary

Subsidence caused by groundwater pumping in the Central Valley has been a problem for decades. Over the last few years, interferometric synthetic aperture radar (InSAR) has been used from satellites and aircraft to produce maps of subsidence with sensitivity of fractions of an inch. For this study, we have obtained and analyzed Japanese PALSAR data for 2006 - 2010 and Canadian Radarsat-2 data for the period May 2014 – January 2015 and produced maps of the total subsidence for those periods. As multiple scenes were acquired during these periods, we can also produce time histories of subsidence at selected locations and transects showing how subsidence varies both spatially and temporally. Geographic Information System (GIS) files will be furnished to DWR for further analysis of the 4 dimensional subsidence time-series maps.

For both periods, two already known main subsidence bowls in the San Joaquin Valley have been mapped: The larger is centered on Corcoran and extends 60 miles to the NW, affecting the California Aqueduct. For the period 2006 - 2010, maximum total subsidence was found to be about 37" near Corcoran. From May 2014 – January 2015, maximum subsidence of over 13" was found just SE of Corcoran. A second bowl is centered on El Nido and is approximately 25 miles in diameter, encompassing most of the East Side Bypass. From 2006 - 2010 maximum subsidence totaled about 24" S of El Nido. From May 2014 – January 2015, maximum subsidence of about 10" occurred in the same area. In the Sacramento Valley, a single area N of Yolo subsided about 6" from 2006 - 2010. From May to November 2014, an extended area W of Yolo showed small areas with a maximum subsidence of about 3"; another diffuse area N of Yolo had a maximum subsidence of about 2.5"; and an unusually small intense area of subsidence just W of Arbuckle showed a maximum subsidence of about 5".

InSAR data were also collected by the NASA UAVSAR airborne platform over two swaths centered on the California Aqueduct to evaluate subsidence on or near the aqueduct using a high spatial resolution instrument. The first swath covered the California Aqueduct from San Luis Reservoir to Kettleman City, and the second from due west of Buttonwillow to the Edmonston Pumping Plant. Time series analysis showed subsidence to be highly variable across this extent and to have increased sharply starting in summer 2014. Impact on the Aqueduct from groundwater withdrawal is greater in the northern swath. The greatest subsidence directly impacting the California Aqueduct was observed between Huron and Kettleman City, where a subsidence bowl of depth about 14" was centered less than half a mile from the Aqueduct. The subsidence bowl extended beyond the aqueduct and caused >8" of subsidence along a 1.3 mile stretch of the aqueduct, with a maximum of about 13" subsidence. We note that subsidence values measured with UAVSAR InSAR are averaged across a pixel of area > 20' x 20', so maximum values measured on the ground could be higher at locations within the pixel.

Introduction

The problem of subsidence

The aquifer system of the southern Central Valley has both unconfined and confined parts caused by alternating layers of coarse and fine-grained sediments. Water in the coarse-grained, unconfined or water-table aquifers can be extracted or recharged easily and causes only minor 'elastic' compaction reflected as seasonal subsidence and rebound of water levels and the land surface. Most water wells exploit the deeper confined aquifers, and withdrawal of water from them causes drainage of the fine-grained confining layers called aquitards. Significant water is available in the aquitards. These, however, drain slowly and compact both elastically as well as inelastically. In general, if water levels are not drawn too low, when pumping ceases water recharges the aquitards and their structure expands. However, if water levels are drawn too low, then an irreversible compaction of the fine-grained aquitards occurs. The water cannot recharge the layers, causing permanent subsidence and loss of some groundwater storage capacity (see Galloway et al., 1999 pages 8-13; Bertholdi et al., 1991 for reviews).

Measuring and understanding subsidence as a function of groundwater dynamics will greatly improve management of that important resource, and in addition the effect of subsidence on infrastructure can also be monitored using InSAR. Roads can be broken by fissures, pipelines have been exhumed, and the slope of the land can be altered, changing drainage patterns. This last effect has proven to be a significant problem on the California Aqueduct, where the canal lining has been raised in multiple locations over the years in order to preserve flow. Areas of low relief that have subsided are also subject to flooding.

How InSAR works

Key points:

1) InSAR measures subsidence relative to a stable location chosen during processing.
2) InSAR measures subsidence relative to the first image date in a series.
3) Radar measurements from multiple satellites can not be combined interferometrically.
4) However, subsidence measurements may be combined if they overlap in time.

Interferometric synthetic aperture radar (InSAR) is a technique whereby surface change occurring between two radar imaging passes may be measured and mapped to high precision (see Madsen and Zebker, 1998; Massonnet, 1997 for reviews). The ability to map surface deformation of a fraction of an inch over large areas at spatial resolutions of 100 feet or so has opened up new possibilities for remote monitoring of groundwater resources. Most applications have used satellite radar systems, although airborne systems are also available.

The technique works by acquiring images from the same viewing geometry at two different times between which a change in the surface position has occurred. The phases of the returning radar waves from the two acquisitions are subtracted to create a phase-difference map, or interferogram, that can be processed to create a map of changes in

distance along the line-of-sight direction that are precise to fractions of the radar wavelength (typical wavelengths are 1-10 inches). There are however some noise factors which must be considered: orbital error, atmospheric noise, topography error and phase decorrelation error. Orbital and topography errors are largely handled in the InSAR data processing. Atmospheric water vapor and other variations in Earth's troposphere can introduce phase delay artifacts that mimic surface changes. This is usually dealt with by analyzing many interferometric pairs and averaging (stacking) assuming ground deformation is steady and atmospheric phase is random in time. For time-varying deformation signals, more sophisticated spatiotemporal filtering can be applied during InSAR time series analysis to mitigate the effects of atmospheric noise (e.g., Galloway et al., 1998; Lanari et al., 2004; Ozawa and Ueda, 2011; Chaussard et al., 2013). Another problem, especially acute in agricultural areas like the Central Valley, is small-scale surface changes near the scale of the radar wavelength. Crops blowing in the wind or fields plowed between radar image acquisitions can spoil the phase coherence between the two radar images and cause loss of information. This effect can be ameliorated by using a longer wavelength and selecting interferometric pairs that have small orbital baseline separations and temporal differences.

After many pairs of radar images over an area have been processed into interferograms, they can be further analyzed to create a time series of surface deformation. This is done by an InSAR time series inversion algorithm called the Small Baseline Subset (SBAS) method (e.g., Berardino et al., 2002; Sansosti et al., 2010). SBAS makes use of interferometric pairs that have small spatial baselines and short temporal separations. The time series is constructed pixel by pixel and requires no assumptions on the continuity or stability of phase in time. Proper choice of the reference location is needed in order to tie together the relative InSAR measurements into a consistent reference frame. The reference location (or pixel) is usually chosen at a place that is stable compared to the deformation of interest based on *in situ* geodetic measurements or *a priori* information.

The InSAR time series analysis produces a history of line-of-sight (LOS) surface displacements similar to GPS time series observations but with much higher spatial resolution. Unlike stacking, which has no temporal resolution, InSAR time series recover both long-term mean velocities, and time varying components, while at the same time isolating atmospheric delays (as well as surface deformation) into the respective SAR image epochs (e.g., Lanari et al., 2004). This technique has been applied successfully for imaging non-steady-state deformation at volcanoes (Lundgren et al., 2004), deforming plate boundaries (Lundgren et al., 2009), and aquifer dynamics (Farr and Liu, 2015; Farr, 2011; Lanari et al., 2004). After the initial time series inversion, temporal and spatial filtering can be applied to further suppress atmospheric noise and smooth the deformation time series. Since atmospheric noise is spatially correlated but temporally uncorrelated, its net effect on the InSAR time series is negligible. The estimated measurement precision for InSAR time series is generally a small fraction of a wavelength, depending on the InSAR acquisitions and noise levels (e.g., Galloway et al., 1998; Ozawa and Ueda, 2011; Chaussard et al., 2013). In the case of the Radarsat-2 measurements shown later, uncertainties associated with the vertical displacement (subsidence/uplift) measurements were determined to be less than 1" and usually less than 0.5". These uncertainties cover random

errors, but do not include systematic errors related to choice of reference location or unwrapping errors.

A final step in post-processing is to use the assumption that subsidence is mainly in the vertical direction, so the line-of-sight measurement from the radars can be projected to the vertical. This allows measurements from multiple satellites to be compared with each other and with GPS and traditional surveying data.

Several groups have made studies of the effects of groundwater withdrawal and recharge on InSAR measurements of deformation of the Earth's surface (e.g. Reeves et al., 2011; Calderhead et al., 2011; Lu and Danskin, 2001; Amelung et al., 1999). Preliminary evaluations of InSAR applications to groundwater monitoring have been made over the last few years in Los Angeles (Bawden et al., 2001), the Antelope Valley (Galloway et al., 1998), Las Vegas (Hoffmann et al., 2001; Bell et al., 2008), the Santa Clara Valley (Sneed et al., 2003), the Coachella Valley (Sneed and Brandt, 2007), and the southern Central Valley (Farr and Liu, 2015; Farr, 2011; Sneed et al., 2013; Borchers and Carpenter, 2014).

A number of satellite systems have been flown over the years to provide InSAR data (Table 1). Note that while the satellites span only a few years each, they overlap in time allowing their time series to be compared. That is a focus of ongoing research in our group at JPL. For this report, PALSAR images spanning the period June 2007 – December 2010 and Radarsat-2 images for the period May 2014 – January 2015 were processed to two independent time series. Details of the data used are listed in the Appendix. Further work under this task will fill the gap between the PALSAR and Radarsat-2 results using Radarsat-1 data.

Satellite	dates	resolution (m)	swath (km)	incidence angles	minimum revisit (days)	band*/pol
ERS 1,2	1991-2010	25	100	25°	35	CVV
Envisat	2002-2010	25	100	15-45°	35	CVV, CHH
PALSAR	2006-2011	10-100	40-350	10-60°	46	L-quad
Radarsat 1	1995-2013	10-100	45-500	20-49°	24	CHH
Radarsat 2	2008-	3-100	25-500	10-60°	24	C-quad
TerraSAR-X	2007-	1-16	5-100	15-60°	11	X-quad
Cosmo-Skymed	2007-	1-100	10-200	20-60°	<1	X-quad
PALSAR-2	2014-	3-60	50-350	8-70°	14	L-quad
Sentinel-1A	2014-	20	250	30-45°	12	C-dual
NISAR	2020?	35	350	15-60°	12	L-quad

* wavelengths: X ~ 3 cm, C ~ 5 cm, L ~ 25 cm

Table 1. Past, present, and future radar satellites.

UAVSAR, which is an L-band SAR flown on a G-3 aircraft, has a much higher signal-to-noise ratio than satellite SARs, usually achieving a factor of 100 increase in signal through the use of a high-power instrument transmitting from 41,000 ft. altitude rather than from Earth orbit. It also has higher spatial resolution than the satellite SARs, with <6' single-look resolution, which allows higher resolution following spatial averaging to reduce the phase noise. The reduction in phase noise means that deformation measurement accuracy is increased and temporal decorrelation is reduced. The practical outcome is that a larger proportion of a UAVSAR scene will produce useful measurements. Previous InSAR results from UAVSAR include measurements of fault slip in California (Donnellan et al., 2014), landslides along the San Andreas fault (Scheingross et al., 2013), and sinkhole precursory ground movement in Louisiana (Jones and Blom, 2014).

UAVSAR data processing followed similar steps to those used for the satellite data. We eliminated very low coherence areas from the analysis by masking out pixels with average coherence less than 0.285 or with coherence < 0.60 in all interferograms. The average is taken over the interferometric coherence associated with each interferogram in the stack. This masking step eliminated most open water and land areas that experienced high and persistent temporal decorrelation. A temporal filter of width 1 month was applied to smooth the results; this value was chosen to be sufficiently short that we are able to resolve when subsidence rates changed during 2014. Pixels were classified based upon their average coherence, and adaptive spatial filtering was applied such that low coherence areas were averaged with nearby same-class pixels to reduce noise, and high coherence pixels were not averaged at all. Uncertainties in the derived subsidence values were obtained through a Jacknife resampling procedure whereby the SBAS processing was run on the stack with data from a single acquisition removed, repeated with removal of each acquisition date in the series. This procedure estimates the combined effect of random errors and systematic errors associated with a single acquisition. The uncertainties in the cumulative subsidence derived from UAVSAR InSAR are in the range of 0.25" to 1.0" across most of the imaged area. Estimates for each pixel are included in the GIS products provided to DWR, and shown in plots in an appendix to this document.

The UAVSAR data analysis methods used in this work are based on procedures developed to monitor the levees in the Sacramento-San Joaquin Delta using the instrument (Jones et al., 2011; 2012; 2015). Unlike in the Central Valley, groundwater pumping is not a problem in the Sacramento-San Joaquin Delta. However, subsidence from aerobic oxidation of the soil and compaction of the soil from pumping to remove water from the upper layers of the soil is common throughout the area (Deverel and Leighton, 2010).

San Joaquin Valley Subsidence

Maps of subsidence in the San Joaquin Valley were made for the period June 2007 – December 2010 (Fig. 1; PALSAR) and May 2014 – January 2015 (Fig. 2; Radarsat-2). Two main subsidence bowls can be seen in the maps of total subsidence: one in the Tulare basin centered on Corcoran and one S of the town of El Nido. The maximum total subsidence for the earlier period in the Tulare Basin was over 37" near Corcoran. The maximum subsidence S of El Nido was approximately 24". During the more recent period, we see that, while the two bowls are generally similar, some of the details have changed. The largest

subsidence S of Corcoran totals over 13” while another diffuse area is located NW of Corcoran with a subsidence of up to 9”. Subsidence of over 3” extends W to the California Aqueduct. This southern subsidence bowl is about 60 x 25 miles. The other main subsidence bowl S of El Nido subsided about 5-6” with pockets up to 10”. The East Side Bypass runs right through the main part of the subsidence in this area.

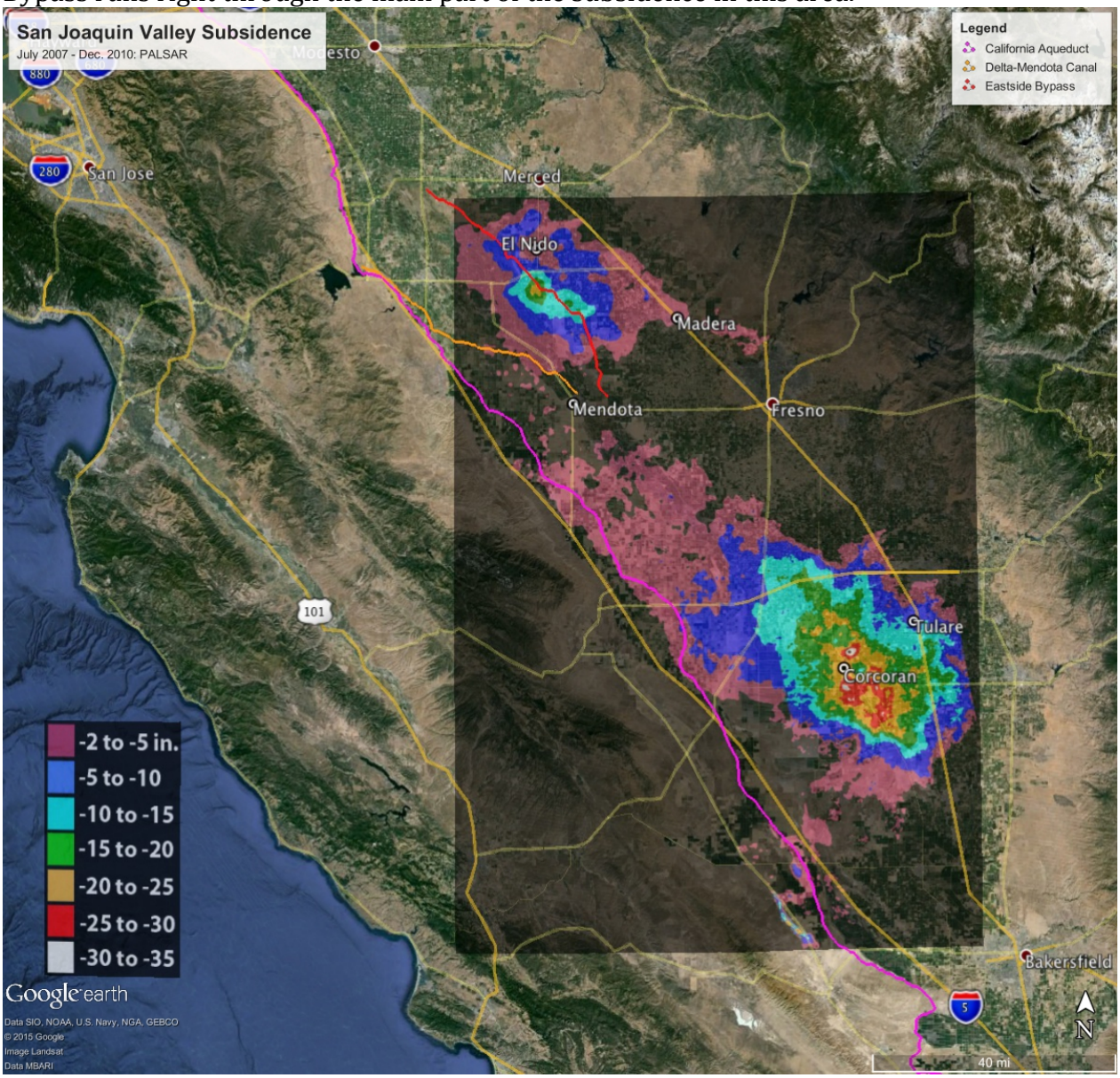

Figure 1. Total subsidence in the San Joaquin Valley for the period June 2007 – December 2010 as measured by the Japanese PALSAR and processed at JPL. Two large subsidence bowls are evident centered on Corcoran and S of El Nido. Note the narrow banana-shaped subsidence feature at bottom center. That corresponds to the Belridge Oil Field, which is subsiding due to oil extraction (Fielding et al., 1998). An animation of the subsidence in the Tulare basin can be seen at: http://photojournal.jpl.nasa.gov/catalog/PIA16293.

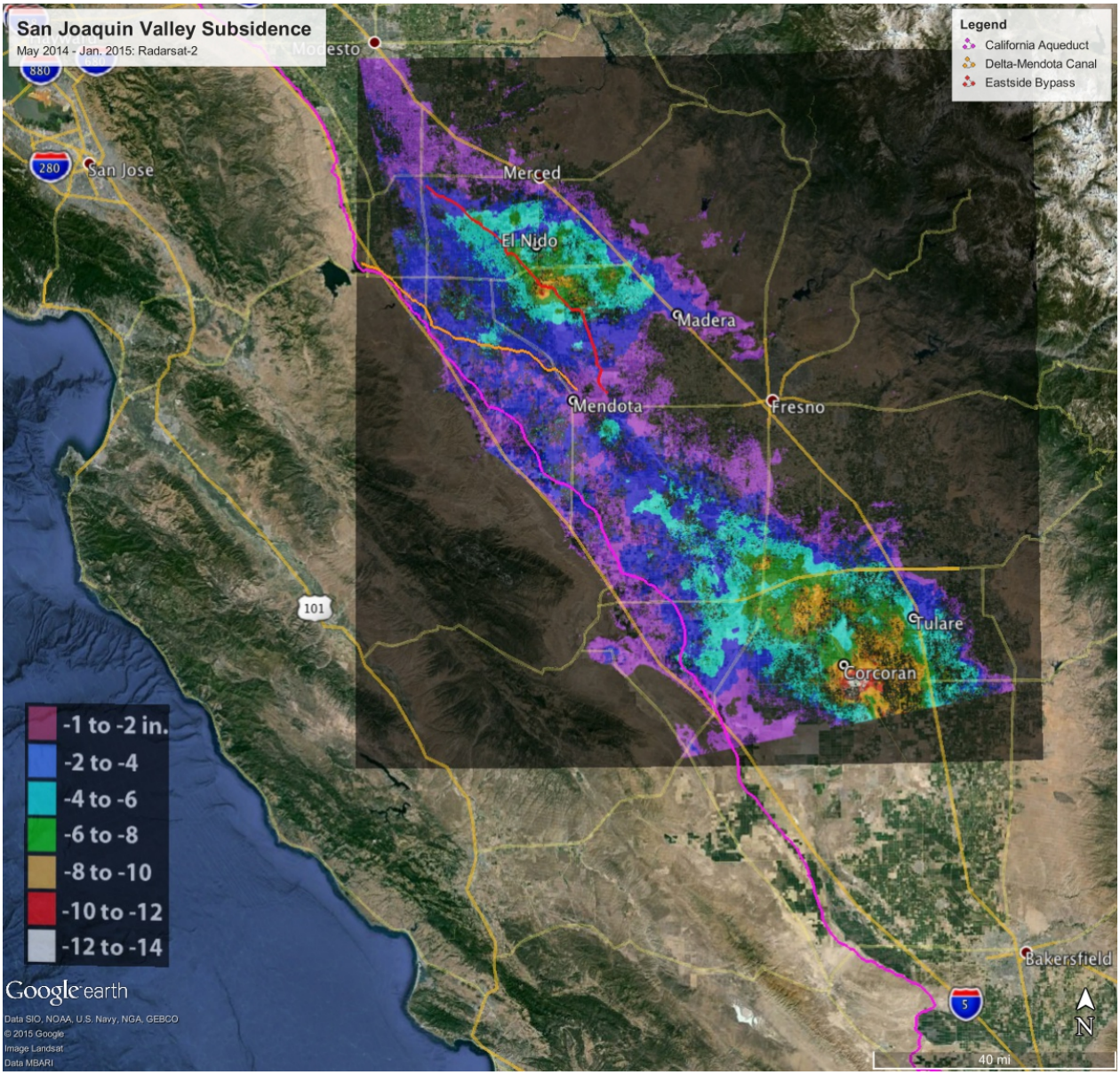

Figure 2. Total subsidence in the San Joaquin Valley for the period 3 May 2014 – 22 January 2015 as measured by the Canadian Radarsat-2 and processed at JPL. The same two large subsidence bowls visible in Figure 1 at Corcoran and El Nido are clearly visible. A preliminary version of this map was presented as Figure 15 in the recent Public Update for Drought Response (CDWR, 2014).

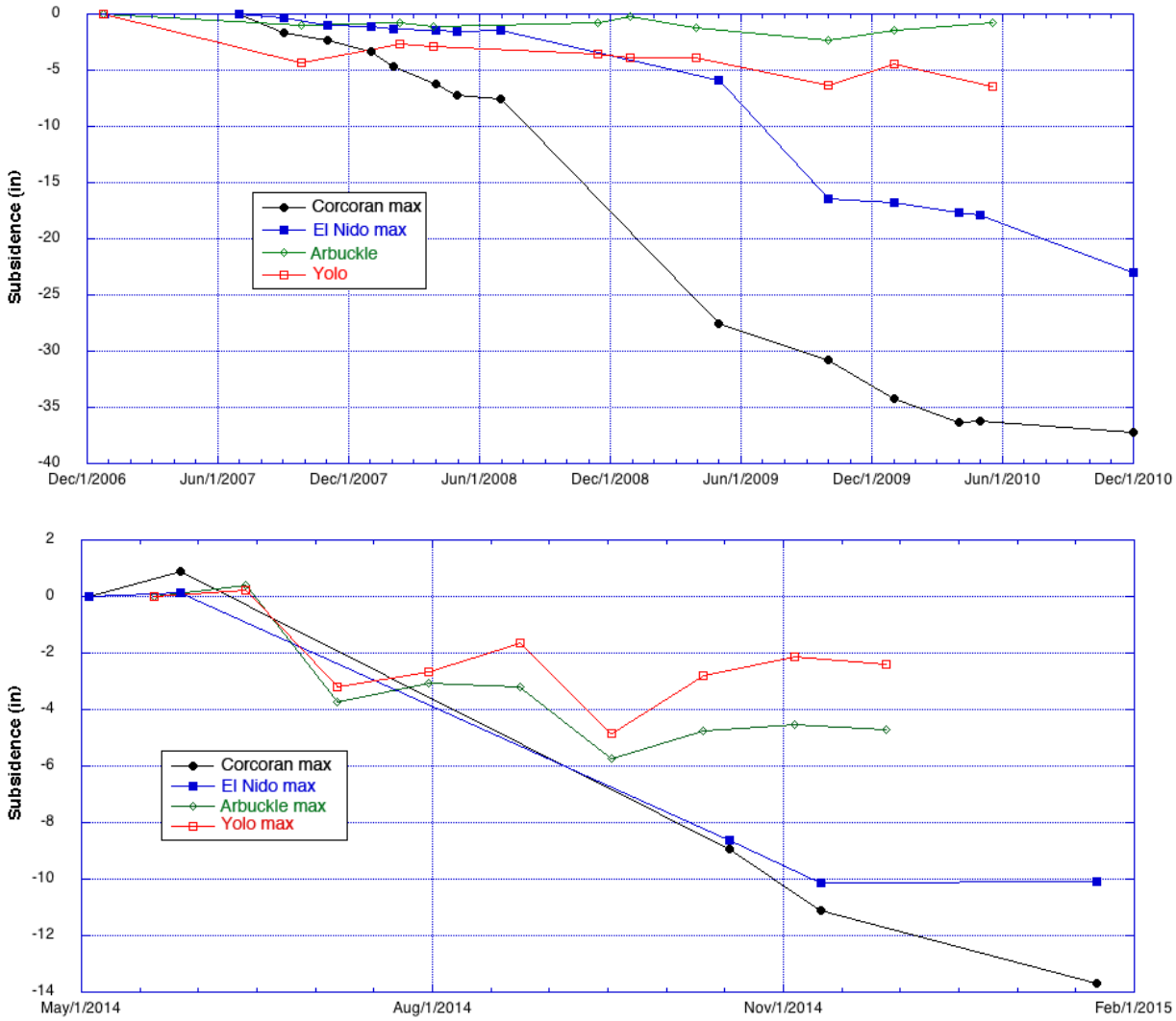

Figure 3. Subsidence histories of a few locations in the San Joaquin and Sacramento Valleys. Top: 2006 – 2010 (PALSAR); Bottom: May 2014 – Jan. 2015 (Radarsat-2). Corcoran max is located in the maximum subsidence pocket just N of Corcoran. El Nido max is located in the pocket just S of El Nido. Arbuckle is located just W of the town of Arbuckle in the Sacramento Valley and Yolo is at the center of the subsidence feature N of Yolo (Fig. 5).

The deformation histories of a few selected locations in the San Joaquin Valley are plotted in Figure 3. The large maximum subsidence in the Corcoran area is clear and shows virtually no recovery at any time in either period of measurement, although the rate seems to decrease in 2010. Likewise, the maximum subsidence location near El Nido shows little seasonal change except for some flattening in 2010 and January 2015. The histories for Arbuckle and Yolo are discussed later in the Sacramento Valley section.

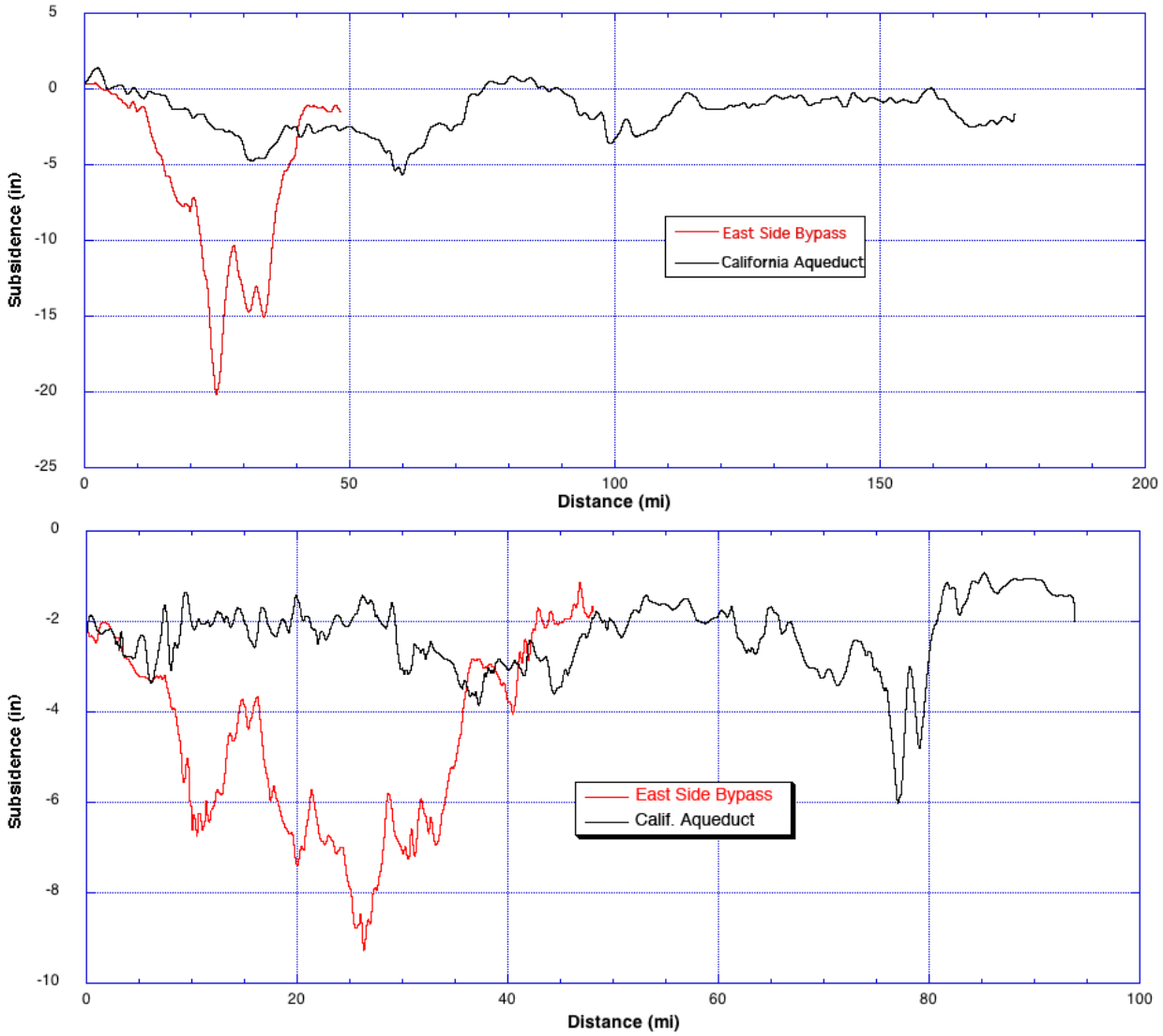

Figure 4. Transects showing total subsidence in the vicinity of the California Aqueduct and the East Side Bypass. The transects extend from N to S with the end points located where the canals intersect the radar images. Top: Total subsidence from June 2007 – December 2010 (PALSAR). Note the deep subsidence pit about midway along the East Side Bypass. That corresponds to the orange area on the map (Fig. 1). Bottom: total subsidence from 3 May 2014 – 22 January 2015 (Radarsat-2). Note the deep subsidence pit about midway along the East Side Bypass. That corresponds to the orange and red area on the map (Fig. 2). The two sharp pits between miles 75 and 80 on the California Aqueduct correspond to the features observed by UAVSAR (Fig. 12).

The transects shown in Figure 4 give a more detailed picture of the total subsidence measured in the vicinity of the California Aqueduct and the East Side Bypass over the two periods of measurement. It is clear that the East Side Bypass has suffered much more subsidence, concentrated in its central area. In contrast, areas in the vicinity of the California Aqueduct experienced up to 5" of subsidence in 2006 - 2010, and a similar amount in the May 2014 – January 2015 time period. These amounts correspond to averages over the processed pixel, not the values on the aqueduct structure itself.

One new concentrated zone along the California Aqueduct stands out in Figure 4, between 75 and 80 miles. This subsidence area appears to be a new zone, and was detected at higher spatial resolution by UAVSAR, as discussed later in this report.

Sacramento Valley Subsidence

Subsidence maps for the southern part of the Sacramento Valley were also produced for this report, covering the period December 2006 to May 2010 (PALSAR; Fig. 5) and 20 May 2014 to 28 November 2014 (Radarsat-2; Fig. 6). Only one area of significant subsidence was detected and mapped in the earlier period: just N of Yolo a bowl about 7 miles across had a maximum subsidence of about 6". This matches well with subsidence mapped by GPS survey from 1999 - 2005 and reported in D'Onofrio and Frame (2006).

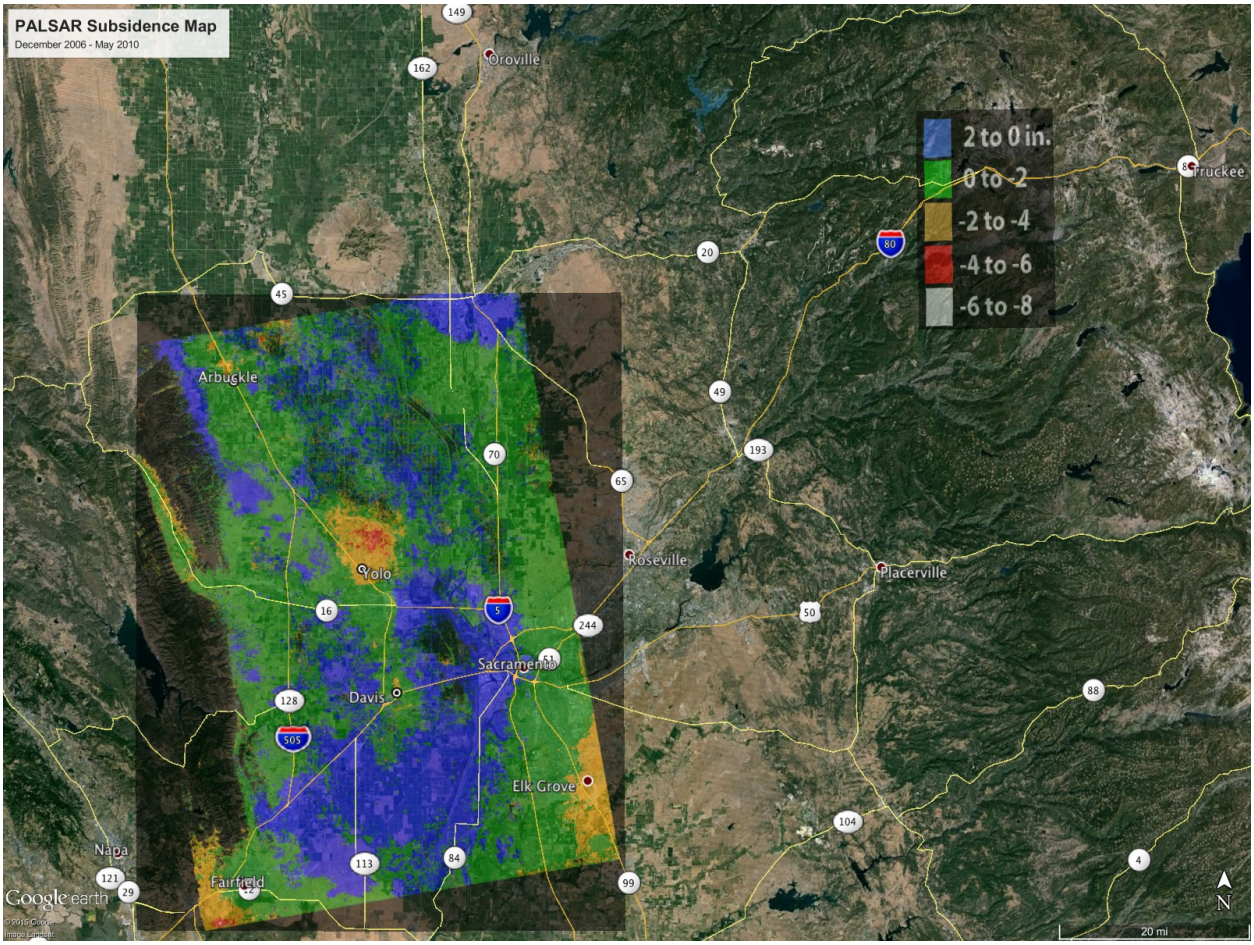

Figure 5. Total subsidence in the Sacramento Valley for the period Dec. 2006 - May 2010 as measured by the Japanese PALSAR and processed at JPL. One subsidence bowl is shown north of Yolo.

The Radarsat-2 map (Fig. 6) shows 3 areas of significant subsidence between 20 May 2014 to 28 November 2014: an extended area W of Yolo includes small areas with a maximum subsidence of about 3"; another diffuse area N of Yolo had a maximum subsidence of about 2.5"; and an unusually small heavily subsiding area just W of Arbuckle showed a maximum subsidence of about 5".

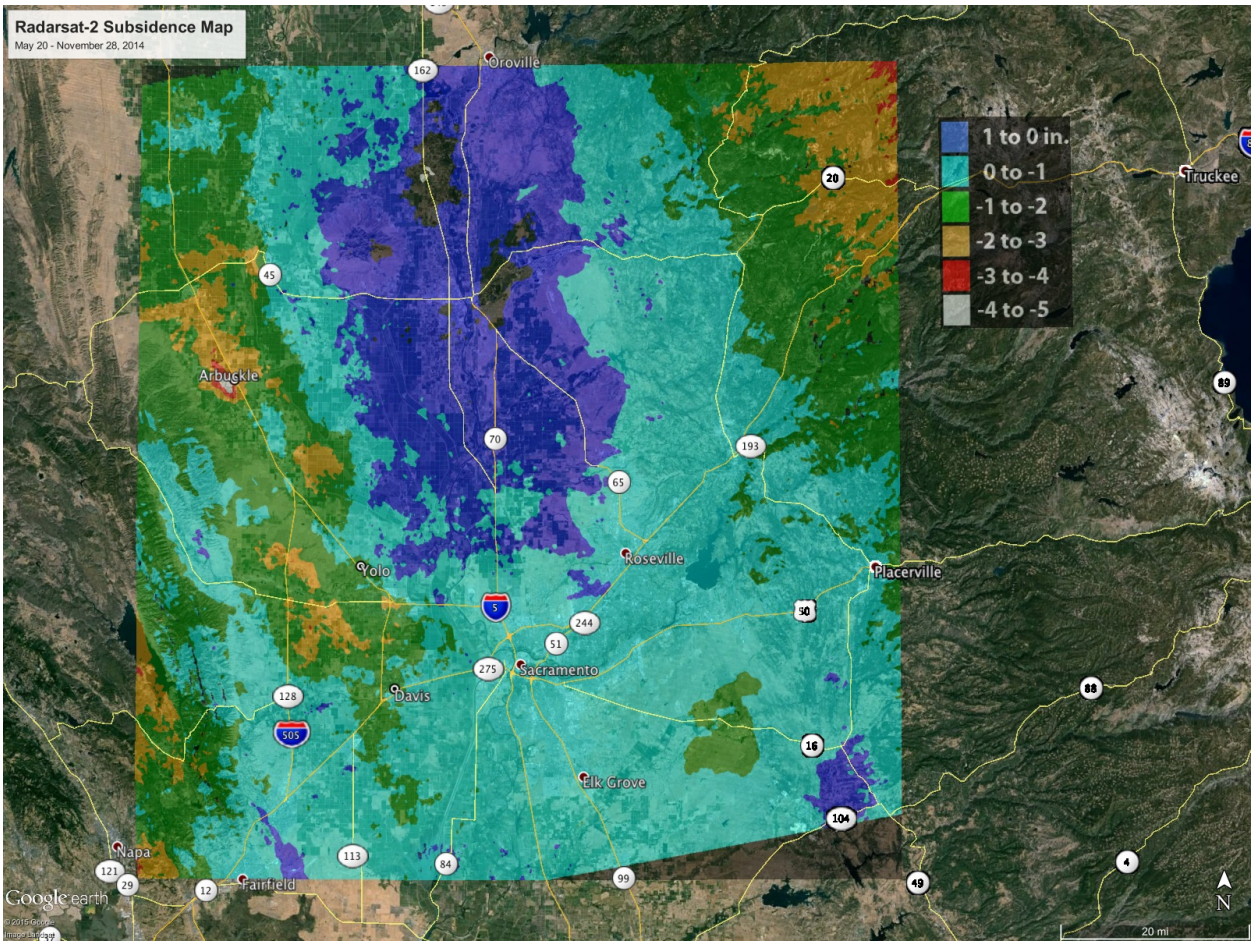

Figure 6. Total subsidence in the Sacramento Valley for the period 20 May 2014 – 28 November 2014 as measured by the Canadian Radarsat-2 and processed at JPL. Two diffuse subsidence areas can be seen west and north of Yolo and a small, deep subsidence bowl is evident just west of Arbuckle.

Subsidence histories of two locations in the Sacramento Valley are shown in Figure 3. The area of maximum subsidence in the PALSAR data north of Yolo (Fig. 5) totals about 6" over the earlier 3.5 year period and about 2" in the last half of 2014. The small area of intense subsidence evident near Arbuckle in 2014 (Fig. 6) shows an uneven subsidence with time in Figure 3, totaling about 5" for the last half of 2014, but no subsidence in 2006 - 2010.

UAVSAR Results Along California Aqueduct

Figure 7 shows the areas in the Central Valley covered by the two UAVSAR flight lines, and the measured subsidence in both imaged areas. The swath to the north showed locations experiencing significantly greater subsidence than was observed in the southern swath. Figure 8 shows only the northern imaged swath. In this stretch of the aqueduct there is an extended region of subsidence in the center, an area of very high subsidence with a very well-defined locus to the south, and several other areas showing subsidence of 3"-5". These areas are shown in more detail in Figures 9-11, where time histories of individual points made clear that even though the northern swath (line 14511) was imaged for a longer

period of time than the southern swath (line 13300), this is not the reason why higher cumulative subsidence was measured there.

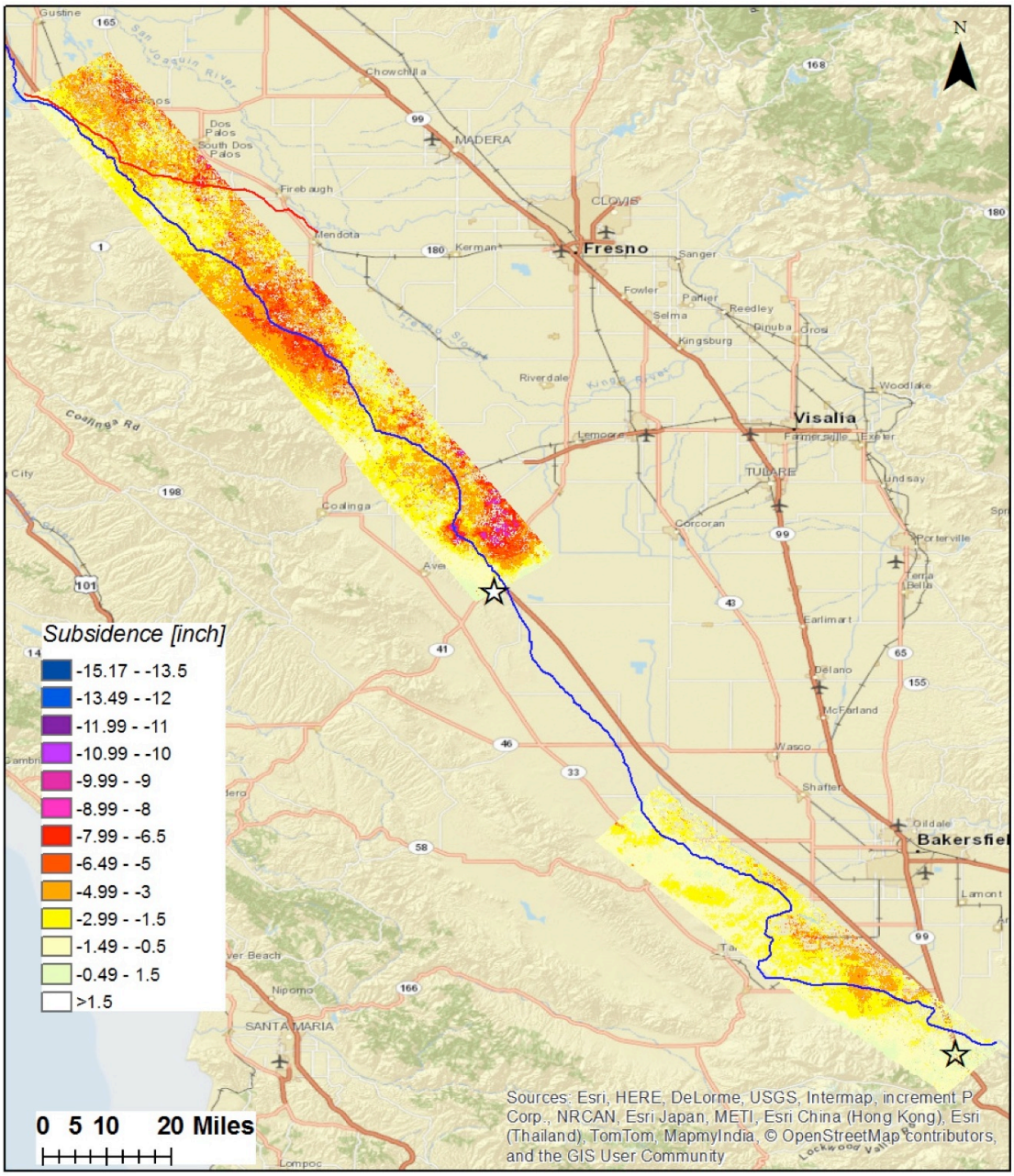

Figure 7. Overview of area in the Central Valley imaged with UAVSAR, showing the broad patterns of subsidence observed. The areas of significant subsidence encompassing the aqueduct during the imaged time period occur entirely in the northern section .These swaths were planned to well image the California Aqueduct, and therefore miss the large subsidence bowls to the east that were seen in the satellite SAR results. The swath to the north is UAVSAR line 14511 and shows cumulative subsidence between 19 July 2013 and 10 March 2015. The swath to the south is UAVSAR line 13300 and shows cumulative subsidence between 2 April 2014 and 7 January 2015. The stars indicate the reference points used for each line, which are the locations in each swath taken to have experienced no subsidence and against which other locations are compared.

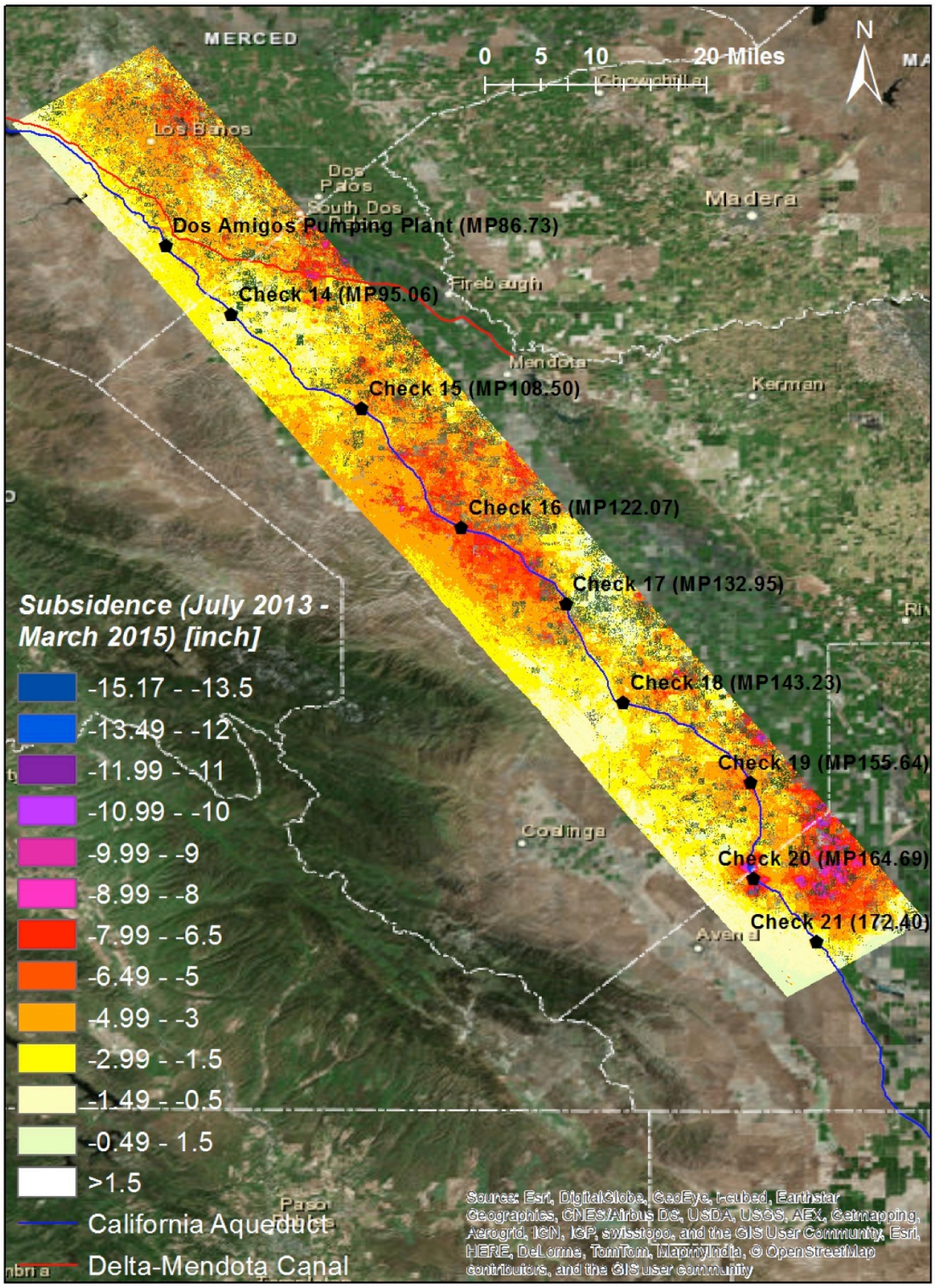

Figure 8. Cumulative subsidence between July 2013 and March 2015 measured with UAVSAR in the Central Valley between San Luis Reservoir and just south of Check 21. A new locus of subsidence, which had the largest aqueduct impact, occurred near Check 20 (see Fig. 9). From south of Check 15 to Check 17 is an area that has historically shown large subsidence of the aqueduct (see Fig. 10). Near Huron (Check 19) is another area of subsidence, this one less extensive in length (see Fig. 11).

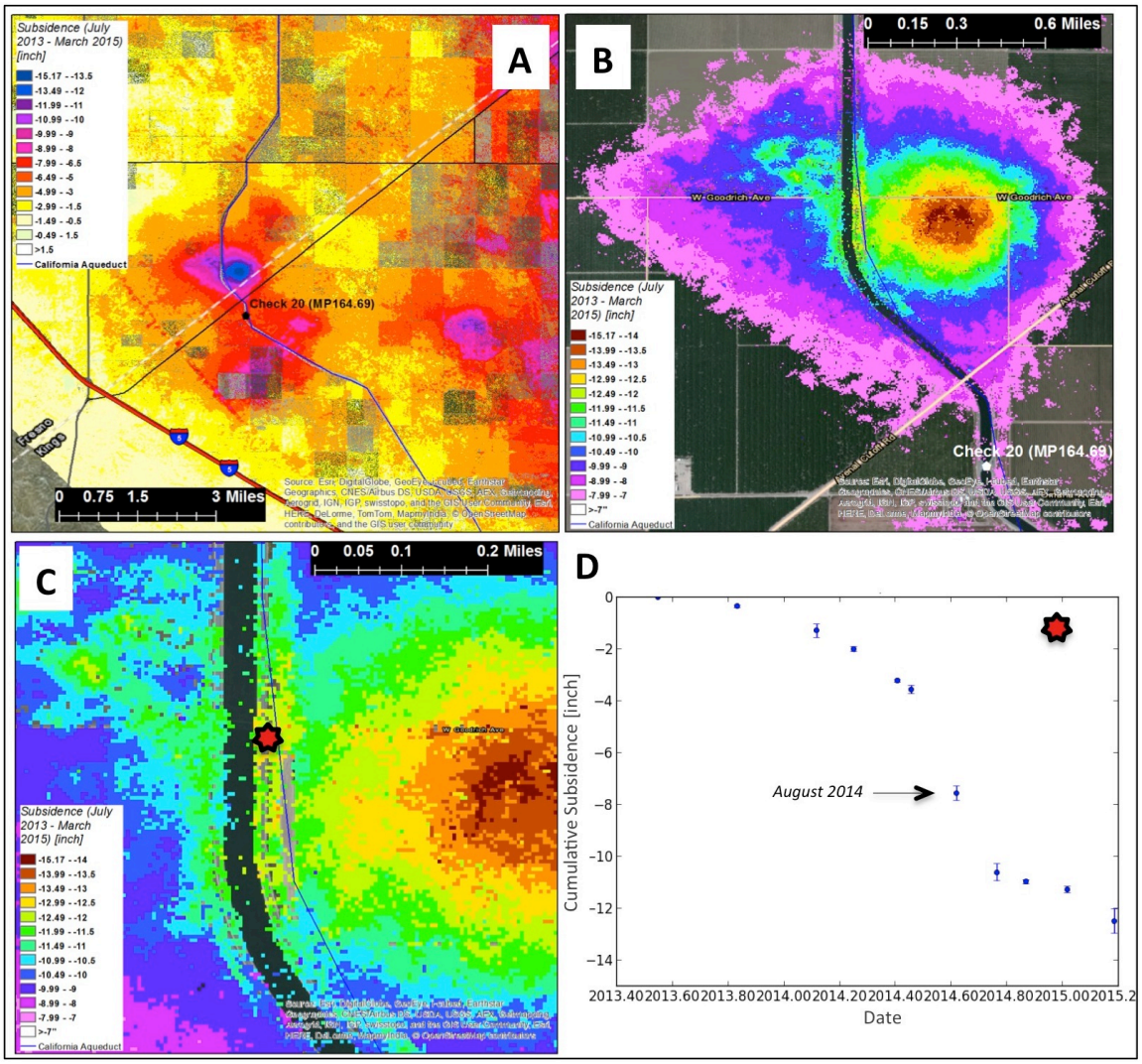

Figure 9. (A) Overview of the cumulative subsidence across an extended area east of Interstate 5, near Check 20 (MP 164.69) at the southern end of swath 14511 (Fig. 8). Several round, localized features are seen in this section, but the one closest to the aqueduct experienced the most subsidence of any area in the two UAVSAR swaths. (B) Enlargement showing the subsidence bowl just north of Avenal Cut-off Road, with a well localized center and extended impact to the surrounding area, including the aqueduct. Limits are placed on the subsidence overlay layer to indicate areas that experienced more than 8" of subsidence between July 2013 and March 2015. Values represent an average over the smoothed pixels, not the maximum subsidence within each pixel. (C) Close-up of the section of the aqueduct nearest the center of the bowl. The star marks the location for which the time history of subsidence is plotted in D. (D) Cumulative subsidence vs. time from July 2013 (zero) to March 2015 (12.5"). This area experienced a dramatic increase in subsidence starting in summer 2014, which slowed abruptly in October 2014.

The greatest subsidence directly impacting the California Aqueduct was observed immediately north of the intersection of the aqueduct with Avenal Cutoff Rd., between Huron and Kettleman City, just north of Check 20 (MP164.69). At this location, a subsidence bowl centered less than half a mile from the aqueduct formed during the study period. Figure 9A shows the subsidence in the vicinity of this location, showing at least three similar features that appear to be associated with wells. Figure 9B shows the locus of the subsidence bowl north of Avenal Cutoff Rd. Limits are placed to indicate the area that experienced >8" of subsidence. The main subsidence bowl impacted the aqueduct significantly, extending from its center in an adjacent field to west of the structure, and caused >8" of subsidence along a 1.3 mile stretch of the aqueduct. In addition, nearly 0.5 miles experienced >11" subsidence (Fig. 9C). Figure 9D shows the temporal development of the subsidence, indicating that high subsidence in this area started around June 2015. The eastern edge of the aqueduct closest to the center of the bowl experienced up to 12.5" of subsidence. The bulk of the subsidence (8") occurred very rapidly, over the period between June and October 2014. There is an indication of increasing subsidence prior to that time, around Feb. 2014, but at a much lower rate than experienced later in the year. The subsidence rate decreased by November 2014. More acquisitions are needed to determine whether the rate is increasing again in March 2015. Comparison with results from Radarsat-2 (Fig. 2, 4) show a larger amount of subsidence measured by UAVSAR, even accounting for the longer time interval covered by the UAVSAR data. This is likely caused by the larger pixel size used in the satellite processing (300' vs. 25') and a slightly longer temporal filter (2 mo. vs. 1 mo.).

Figure 10 shows the cumulative subsidence between Check 16 (MP122.07) and Check 17 (MP132.95) of the California Aqueduct, near Cantua Creek. Although subsidence in this area was less (only up to 8"), a longer stretch of the aqueduct was affected. Similar to the Avenal subsidence bowl, the subsidence rate appears to have increased dramatically in spring 2014, and to have lessened in autumn 2014. Figure 11 shows the area immediately east of Huron, in the vicinity of Check 19 (MP155.64). Unlike the other two areas, subsidence here has been more consistent, albeit with a noticeable but less precipitous increase in rate in spring/summer 2014. Here the cumulative subsidence was about 7" during the 20 months that the area was monitored.

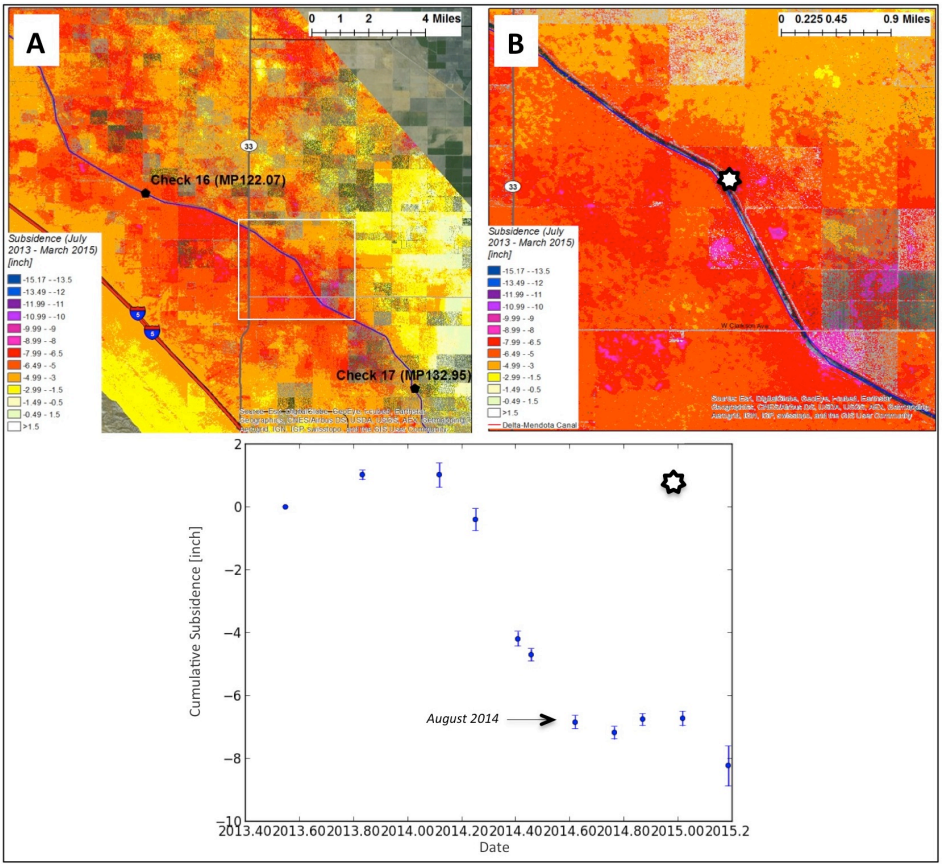

Figure 10. (A) Subsidence in the Cantua Creek area, showing an extended section of the California Aqueduct encompassing Checks 16 and 17 that experienced as much as 8" of subsidence between July 2013 and March 2015. The time series shows that in this area there is seasonal uplift/subsidence and that the subsidence accelerated in spring 2014 and tapered off in fall 2014.

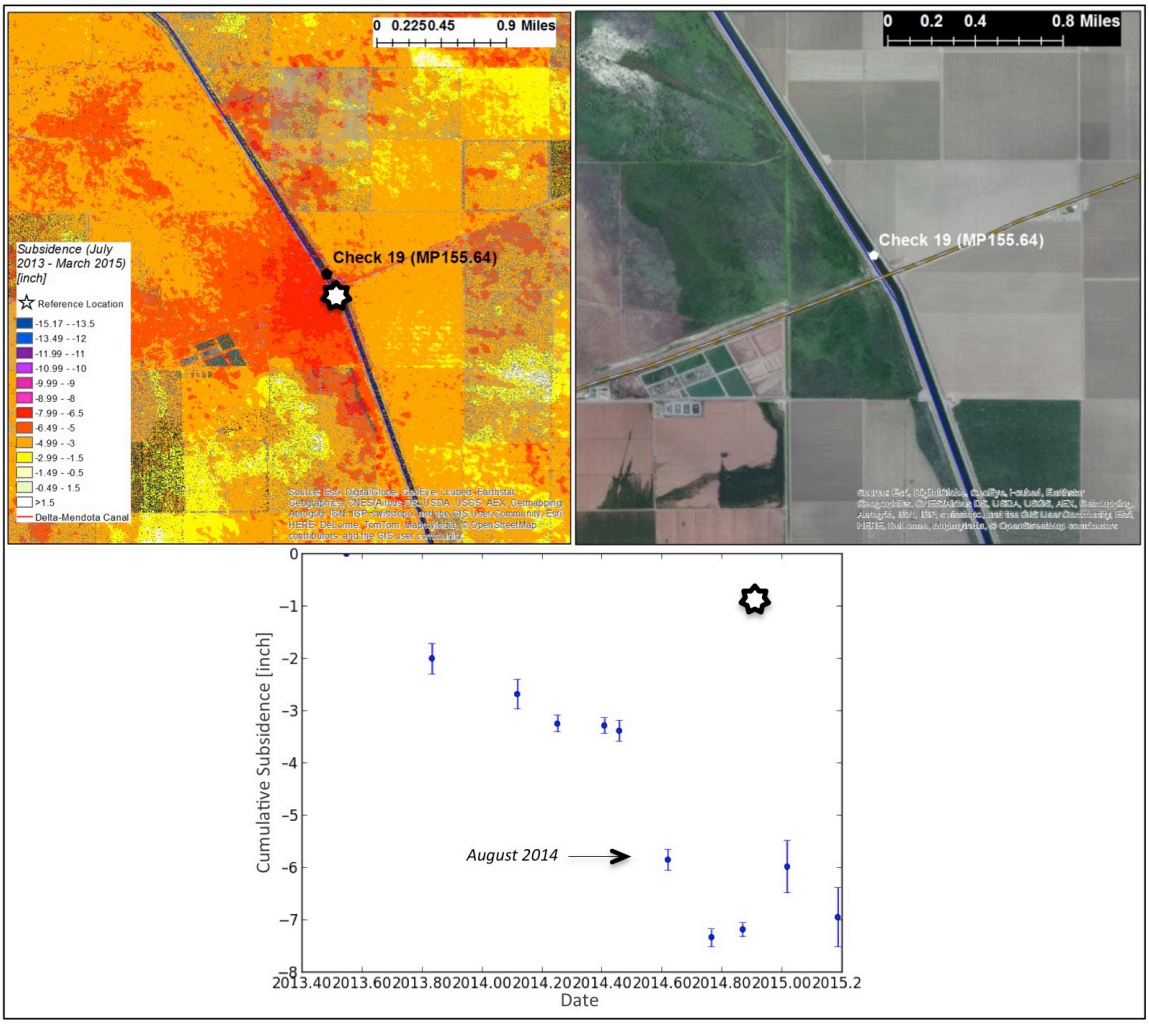

Figure 11. Location immediately east of Huron where a short stretch of the California Aqueduct has experienced nearly steady subsidence since July 2013, accumulating about 7" of vertical displacement between July 2013 and March 2015. There is larger uncertainty at the last two time steps, which can be decreased with additional UAVSAR acquisitions.

Figure 12 shows subsidence in the southern swath, where only one area indicated particularly anomalous subsidence directly affecting the California Aqueduct. This is near where Old River Rd. crosses the aqueduct, between Check 33 (MP267.36) and Check 34 (MP271.27) (Figure 13). For this line, we have no data prior to April 2014 so we cannot tell whether this is an area showing persistent or recent subsidence. We do observe subsidence in the south-central part of the imaged swath (Fig. 13A), but it did not directly affect the aqueduct during April 2014 – Jan. 2015. No substantial subsidence is seen west of Buttonwillow, although ground subsidence associated with oil extraction is apparent (Fig. 13C).

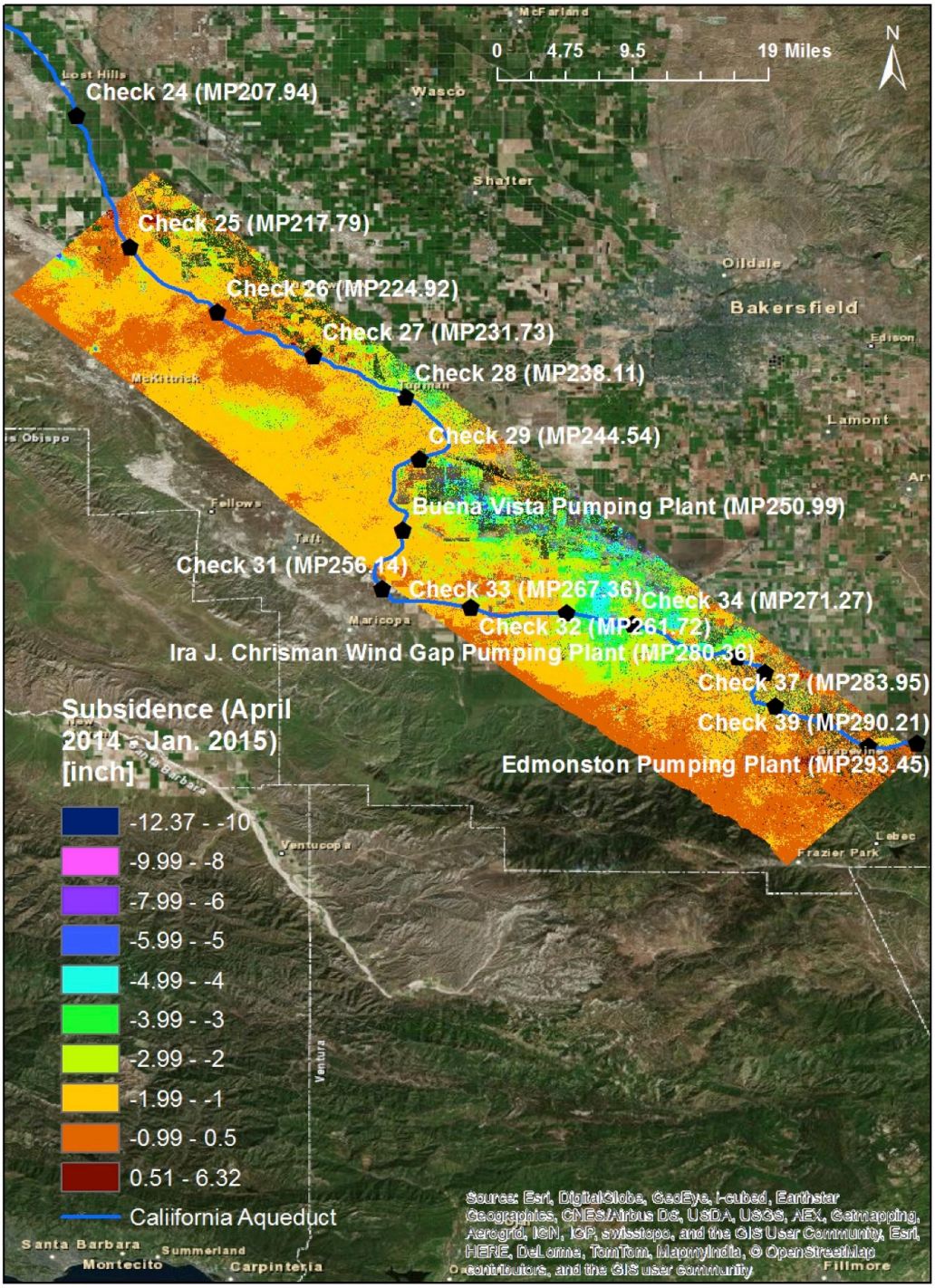

Figure 12. (Top) Cumulative subsidence between April 2014 and January 2015 measured with UAVSAR in the Central Valley between Buttonwillow and the Edmonston Pumping Station. The subsidence is much less in this area than in the area to the north shown in Figure 9.

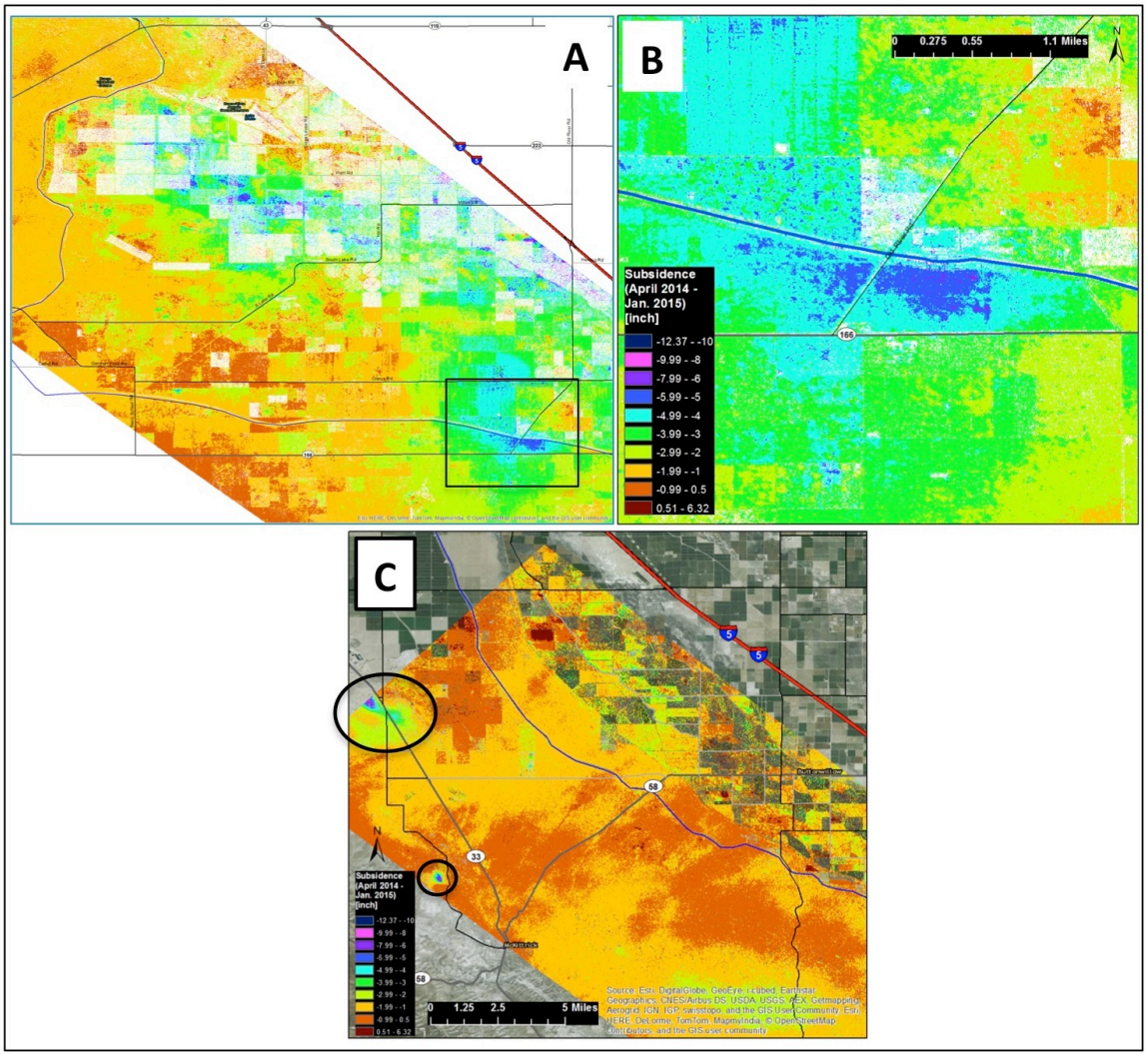

Figure 13. (A) The central section of UAVSAR line 13300 (Fig. 12) showing the greatest subsidence. (B) The one area that showed significant subsidence (outlined in A), with up to 5" on the sides of the aqueduct. (C) North end of line 13300, near Buttonwillow. The only high subsidence in this area occurs near oil fields (circled) and does not impact the aqueduct.

Conclusions and Future Plans

PALSAR and Radarsat-2 have proved to be useful for making maps of Central Valley subsidence. Maps as well as pixel histories of subsidence and transects showing temporal and spatial details of subsidence can be produced from the InSAR data. Updates of the subsidence maps for the Central Valley will continue with the advent of Europe's Sentinel-1A (Table 1). The first acquisitions for the Central Valley were in January 2015 and are continuing, in general every 24 days. Figure 14 shows example coverage of Sentinel-1A.

The UAVSAR results show that radar remote sensing using high resolution, L-band (10" wavelength) SAR can rapidly identify the localized areas of subsidence, so that resources can be targeted efficiently to protect and maintain critical infrastructure. Using UAVSAR,

we were able to locate and monitor a previously unknown locus of subsidence that caused the California Aqueduct to subside by as much as 13", so that further work can be done to identify the cause of the subsidence and prevent it from happening in the future. Furthermore, with frequent monitoring we were able to isolate the time period during which rapid subsidence occurred. Without this kind of comprehensive, rapidly acquired mapping capability it would not be possible to identify through ground surveys alone this type of problem that rapidly developed during the ongoing drought. UAVSAR acquisitions of the two swaths imaging the California Aqueduct are planned to continue for another 6-9 months at least.

As described above, the InSAR time series we produce are essentially series of maps representing the change in surface elevation for each satellite acquisition date. In a sense, we produce 4-dimensional data sets. We have found a convenient format for storage and post-processing is a multi-band GeoTiff format, where each 'band' is an acquisition date. Most common Geographic Information System software packages recognize this format and can display map products from the data. We will furnish all of our products to the DWR in this format for future use and generation of additional products.

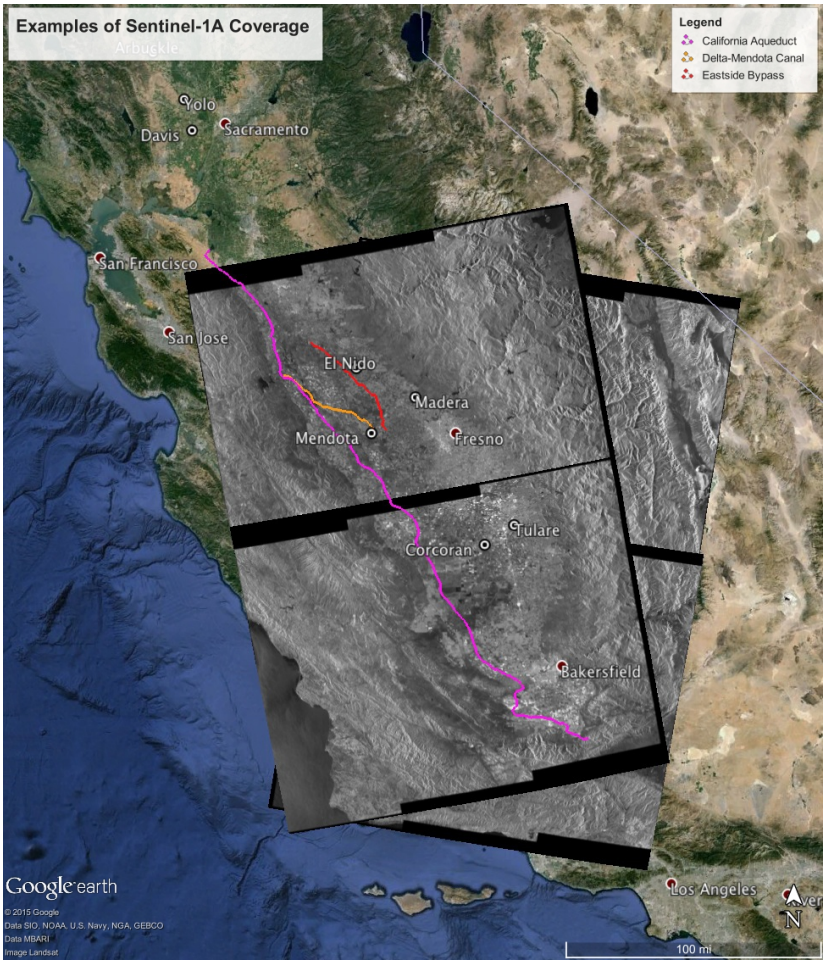

Figure 14. Examples of Sentinel-1A coverage of the San Joaquin Valley. All of California will be covered by this satellite approximately every 24 days from both ascending (SE-NW) and descending (NE-SW) tracks.

Acknowledgements

This work was funded by the California Department of Water Resources. Part of this work was carried out at the Jet Propulsion Laboratory, California Institute of Technology, under contract with NASA. The Alaska Satellite Facility (http://www.asf.alaska.edu/) archives and distributes the PALSAR data used in this study. The Japanese Space Agency contributed the PALSAR data.

References

Amelung, F., D.L. Galloway, J.W. Bell, H.A. Zebker, R.J. Laczniak, 1999, Sensing the ups and downs of Las Vegas: InSAR reveals structural control of land subsidence and aquifer-system deformation, Geology, v. 27, p. 483-486.

Bawden, G.W., W. Thatcher, R.S. Stein, K.W. Hudnut, G. Peltzer, 2001, Tectonic contraction across Los Angeles after removal of groundwater pumping effects, Nature, v. 412, p. 812-813.

Bell, J.W., F. Amelung, A. Ferretti, M. Bianchi, F. Novali, 2008, Permanent scatterer InSAR reveals seasonal an long-term aquifer-system response to groundwater pumping and artificial recharge, Water Resources Research, v. 44, doi: 10.1029/2007WR006152.

Berardino, P., G. Fornaro, R. Lanari, E. Sansosti, 2002, A new algorithm for surface deformation monitoring based on small baseline differential SAR interferograms, IEEE Trans. Geosci. Remote Sensing, v. 40, doi:10.1109/TGRS.2002.803792.

Bertoldi, G.L., R.H. Johnston, K.D. Evenson, 1991, Ground water in the Central Valley, California—A summary report, U.S. Geological Survey Professional Paper 1401-A, 44 p.

Borchers, J.W., M. Carpenter, 2014, Land Subsidence from Groundwater Use in California, Report of Findings to the California Water Foundation, http://www.californiawaterfoundation.org

CDWR, 2014, Public update for drought response, Calif. Dept. Water Resources, Sacramento, 39 pp.

Calderhead, A.I., R. Therrien, A. Rivera, R. Martel, J. Garfias, 2011, Simulating pumping-induced regional land subsidence with the use InSAR and field data in the Toluca Valley, Mexico, Adv. Water Resources, v. 34, p. 83-97, doi:10.1016/j.advwatres.2010.09.017.

Chaussard, E., F. Amelung, H. Abidin, S-H. Hong, 2013, Sinking cities in Indonesia: ALOS PALSAR detects rapid subsidence due to groundwater and gas extraction, Rem. Sens. Env., v. 128, p. 150-161.

Deverel, S.J., D.A. Leighton, 2010, Historic, recent, and future subsidence, Sacramento-San Joaquin Delta, California, USA, San Francisco Estuary and Watershed Science, v. 8.

Donnellan, A., J. Parker, S. Hensley, M. Pierce, J. Wang, J. Rundle, 2014, UAVSAR observations of triggered slip on the Imperial, Superstition Hills, and East Elmore Ranch Faults associated with the 2010 M 7.2 El Mayor‐Cucapah earthquake, Geochemistry, Geophysics, Geosystems, v. 15, p. 815-829.

D'Onofrio, D., J. Frame, 2006, The Yolo County GPS subsidence network: Recommendations and continued monitoring, accessed at http://www.yolowra.org/projects/YSN2005%20Final%20Report.pdf

Farr, T.G., 2011, Remote monitoring of groundwater with orbital radar, abs., Groundwater Resources Assoc. Ann. Mtg., Sacramento, CA. http://www.grac.org/am2011.asp

Farr, T.G., Z. Liu, 2015, Monitoring Subsidence Associated with Groundwater Dynamics in the Central Valley of California Using Interferometric Radar, Ch. 24 in Remote Sensing of the Terrestrial Water Cycle, Geophysical Monograph 206, V. Lakshmi, ed., American Geophysical Union, John Wiley & Sons, Inc.

Fielding, E.J., R.G. Blom, R.M. Goldstein, 1998, Rapid subsidence over oil fields measured by SAR interferometry, Geophys. Res. Lett., v. 25, p. 3215-3218.

Galloway, D.L., D.R. Jones, S.E. Ingebritsen, 1999, Land subsidence in the United States. U.S. Geological Survey Circular 1182, 175 p.

Galloway, D.L., K.W. Hudnut, S.E. Ingebritsen, S.P. Phillips, G. Peltzer, F. Rogez, P.A. Rosen, 1998, Detection of aquifer system compaction and land subsidence using interferometric synthetic aperture radar, Antelope Valley, Mojave Desert, California, Water Resources Research, v. 34, p. 2573-2585.

Hoffmann, J., H.A. Zebker, D.L. Galloway, F. Amelung, 2001, Seasonal subsidence and rebound in Las Vegas Valley, Nevada, observed by synthetic aperture radar interferometry, Water Resources Research, v. 37, p. 1551-1566.

Jones, C.E., R.G. Blom, 2014, Bayou Corne, Louisiana, sinkhole: Precursory deformation measured by radar interferometry, Geology, v. 42, p. 111-114.

Jones, C., G. Bawden, S. Deverel, J. Dudas, S. Hensley, 2011, Characterizing land surface change and levee stability in the Sacramento-San Joaquin Delta using UAVSAR radar imagery, Proc. IEEE Geoscience and Remote Sensing Symposium (IGARSS), p. 1638-1641.

Jones, C.E., G. Bawden, S. Deverel, J. Dudas, S. Hensley, S.H. Yun, 2012, Study of movement and seepage along levees using DINSAR and the airborne UAVSAR instrument, abs. SPIE Remote Sensing, International Society for Optics and Photonics.

Jones, C.E., J. Dudas, G.W. Bawden, 2015, Application of remote sensing to assessment of water conveyance infrastructure integrity, in Anderson, R.L., and Ferriz, H., Applied

Geology in California, Special Publication 26, Association of Environmental and Engineering Geologists, Star Publishing Company, in press.

Jones, J., 2009, California Drought, an update: December 2009, CA Dept. of Water Resources, 112 pp.

Lanari, R., P. Lundgren, M. Manzo, F. Casu, 2004, Satellite radar interferometry time series analysis of surface deformation for Los Angeles, California, Geophys. Res. Lett., v. 31, doi: 10.1029/2004GL021294.

Liu, Z., D. Dong, P. Lundgren, 2011, Constraints on time-dependent volcanic dynamics at Long Valley Caldera from 1996 to 2009 using InSAR and geodetic measurements, Geophys. J. Int., v. 187, p. 1283-1300, doi:10.1111/j.1365-246X.2011.05214.x.

Lu, Z., W.R. Danskin, 2001, InSAR analysis of natural recharge to define structure of a ground-water basin, San Bernardino, California, Geophys. Res. Lett., v. 28, p. 2661-2664.

Lundgren, P., F. Casu, M. Manzo, A. Pepe, P. Berardino, E. Sansosti, R. Lanari, 2004, Gravity and magma induced spreading of Mount Etna volcano revealed by satellite radar interferometry, Geophys. Res. Lett., v. 31, L04602.

Lundgren, P., E. A. Hetland, Z. Liu, and E. J. Fielding, 2009, Southern San Andreas-San Jacinto fault system slip rates estimated from earthquake cycle models constrained by GPS and interferometric synthetic aperture radar observations, J. Geophys. Res., v. 114, B02403, doi:10.1029/2008JB005996.

Madsen, S.N., H.A. Zebker, 1998, Imaging Radar Interferometry, ch. 6, p. 359-380, in Henderson, F.M., A.J. Lewis, ed., 1998, Principles and Applications of Imaging Radar, Manual of Remote Sensing, v. 2, Wiley, NY, 866 pp.

Massonnet, D., 1997, Satellite radar interferometry, Scientific American, v. 276, Feb., p. 46-53.

Ozawa, T., H. Ueda, 2011, Advanced interferometric synthetic aperture radar (InSAR) time series analysis suing interferograms of multiple-orbit tracks: a case study on Miyake-Jima, J. Geophys. Res., 116, B12407, doi:10.1029/2011JB008489.

Reeves, J.A., R.J. Knight, H. Zebker, W.A. Schreüder, P.S. Agram, and T.R. Lauknes, 2011, High quality InSAR data linked to seasonal change in hydraulic head for an agricultural area in the San Luis Valley, Colorado, WRR, v. 47, DOI: 10.1029/2010WR010312.

Sansosti, E., F. Casu, M. Manzo, R. Lanari, 2010, Space‐borne radar interferometry techniques for the generation of deformation time series: An advanced tool for Earth's surface displacement analysis, Geophys. Res. Lett., v. 37, L20305, doi:10.1029/2010GL044379.

Scheingross, J.S., B.M. Minchew, B.H. Mackey, M. Simons, M.P. Lamb, S. Hensley, 2013, Fault-zone controls on the spatial distribution of slow-moving landslides, Geol. Soc. Amer. Bull., v. 125, p. 473-489.

Sneed, M., and Brandt, J.T., 2013, Detection and measurement of land subsidence using global positioning system surveying and Interferometric Synthetic Aperture Radar, Coachella Valley, California, 1996-2005: U.S. Geological Survey Scientific Investigations Report 2007-5251, v. 2.0, 31 p.

Sneed, M., S.V. Stork, R.J. Laczniak, 2003, Aquifer-system characterization using InSAR, in K.R. Prince and D.L. Galloway, eds., US Geological Survey subsidence interest group conference proceedings, 2001, USGS Open-File Rept. 03-308.

Sneed, M., and Brandt, J.T., 2007, Detection and measurement of land subsidence using global positioning system surveying and Interferometric Synthetic Aperture Radar, Coachella Valley, California, 1996-2005: U.S. Geological Survey Scientific Investigations Report 2007-5251, 31 p.

Appendix: Detailed lists of data used

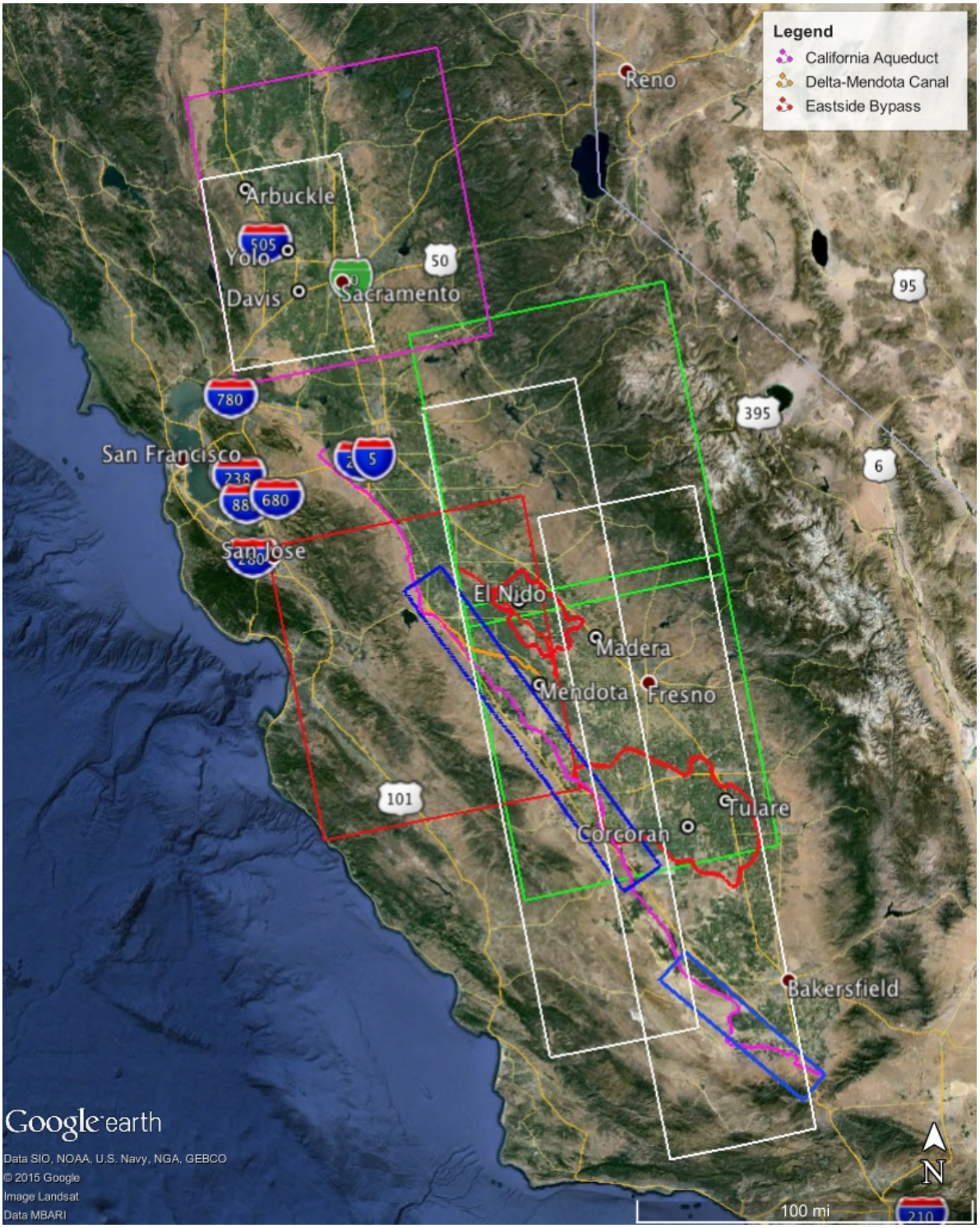

Figure A1. Map showing PALSAR (white), Radarsat-2 (green, red, purple), and UAVSAR (blue) coverage of the Central Valley. Note that the southern edge of the Radarsat-2 tracks (green) was determined by competing data acquisitions by oil companies monitoring subsidence in the oil fields west of Bakersfield. The red box represents the San Joaquin Valley frame of the western track that is not shown in this report.

PALSAR Data Listing

The Phased-Array L-band Synthetic Aperture Radar (PALSAR) of the Japanese Space Agency (JAXA) was used for the earlier data in this report. Data were obtained from the Alaska Satellite Facility (https://www.asf.alaska.edu). See Table 1 for some characteristics of the instrument. Three orbital paths were used, all ascending (SE to NW) and shown in Figure A1: 2 to cover the San Joaquin Valley and 1 for the southern part of the Sacramento Valley. Swaths are broken into frames, which are stitched together in the processing. HH polarization was used for all InSAR products. Details of the frames used are given below.

Table A1. Details of PALSAR frames used for this report.

Granule Name	Orbit	Path	Frame	Acquisition Date	Center Lat	Center Lon	Angle
San Joaquin Valley, East swath							
ALPSRP074860690	7486	218	690	6/21/07 6:26	35.1596	-119.4419	34.3
ALPSRP074860700	7486	218	700	6/21/07 6:26	35.6542	-119.5492	34.3
ALPSRP074860710	7486	218	710	6/21/07 6:26	36.1486	-119.6569	34.3
ALPSRP074860720	7486	218	720	6/21/07 6:26	36.6431	-119.7657	34.3
ALPSRP074860730	7486	218	730	6/21/07 6:26	37.1376	-119.8732	34.3
ALPSRP088280690	8828	218	690	9/21/07 6:26	35.1623	-119.4405	34.3
ALPSRP088280700	8828	218	700	9/21/07 6:26	35.6568	-119.5488	34.3
ALPSRP088280710	8828	218	710	9/21/07 6:26	36.1472	-119.6537	34.3
ALPSRP088280720	8828	218	720	9/21/07 6:26	36.6421	-119.7619	34.3
ALPSRP088280730	8828	218	730	9/21/07 6:26	37.1363	-119.8705	34.3
ALPSRP094990690	9499	218	690	11/6/07 6:25	35.1617	-119.4337	34.3
ALPSRP094990700	9499	218	700	11/6/07 6:25	35.6566	-119.5399	34.3
ALPSRP094990710	9499	218	710	11/6/07 6:25	36.1512	-119.6462	34.3
ALPSRP094990720	9499	218	720	11/6/07 6:26	36.6461	-119.7529	34.3
ALPSRP094990730	9499	218	730	11/6/07 6:26	37.1406	-119.8619	34.3
ALPSRP101700690	10170	218	690	12/22/07 6:25	35.1585	-119.4356	34.3
ALPSRP101700700	10170	218	700	12/22/07 6:25	35.6533	-119.5415	34.3
ALPSRP101700710	10170	218	710	12/22/07 6:25	36.1481	-119.6479	34.3
ALPSRP101700720	10170	218	720	12/22/07 6:25	36.6429	-119.7548	34.3
ALPSRP101700730	10170	218	730	12/22/07 6:25	37.1376	-119.8619	34.3
ALPSRP108410690	10841	218	690	2/6/08 6:24	35.1452	-119.424	34.3
ALPSRP108410700	10841	218	700	2/6/08 6:24	35.6401	-119.5294	34.3
ALPSRP108410710	10841	218	710	2/6/08 6:25	36.1348	-119.6358	34.3
ALPSRP108410720	10841	218	720	2/6/08 6:25	36.6296	-119.7424	34.3
ALPSRP108410730	10841	218	730	2/6/08 6:25	37.124	-119.8496	34.3
ALPSRP115120690	11512	218	690	3/23/08 6:24	35.1622	-119.4257	34.3
ALPSRP115120700	11512	218	700	3/23/08 6:24	35.6571	-119.5324	34.3
ALPSRP115120710	11512	218	710	3/23/08 6:24	36.1516	-119.6384	34.3
ALPSRP115120720	11512	218	720	3/23/08 6:24	36.6465	-119.7451	34.3
ALPSRP115120730	11512	218	730	3/23/08 6:24	37.1408	-119.8525	34.3
ALPSRP121830690	12183	218	690	5/8/08 6:23	35.1633	-119.4195	34.3
ALPSRP121830700	12183	218	700	5/8/08 6:23	35.6581	-119.5264	34.3
ALPSRP121830710	12183	218	710	5/8/08 6:23	36.1531	-119.6324	34.3
ALPSRP121830720	12183	218	720	5/8/08 6:23	36.6475	-119.7391	34.3
ALPSRP121830730	12183	218	730	5/8/08 6:23	37.142	-119.8461	34.3
ALPSRP128540690	12854	218	690	6/23/08 6:22	35.1462	-119.4407	34.3
ALPSRP128540700	12854	218	700	6/23/08 6:22	35.6408	-119.548	34.3

ALPSRP128540710	12854	218	710	6/23/08 6:23	36.1353	-119.656	34.3
ALPSRP128540720	12854	218	720	6/23/08 6:23	36.6299	-119.7628	34.3
ALPSRP128540730	12854	218	730	6/23/08 6:23	37.1241	-119.8719	34.3
ALPSRP135250690	13525	218	690	8/8/08 6:23	35.1617	-119.4842	34.3
ALPSRP135250700	13525	218	700	8/8/08 6:23	35.6563	-119.5923	34.3
ALPSRP135250710	13525	218	710	8/8/08 6:23	36.1507	-119.7007	34.3
ALPSRP135250720	13525	218	720	8/8/08 6:23	36.6453	-119.8085	34.3
ALPSRP135250730	13525	218	730	8/8/08 6:23	37.14	-119.9166	34.3
ALPSRP182220690	18222	218	690	6/26/09 6:27	35.1638	-119.456	34.3
ALPSRP182220700	18222	218	700	6/26/09 6:27	35.6585	-119.5623	34.3
ALPSRP182220710	18222	218	710	6/26/09 6:27	36.1533	-119.669	34.3
ALPSRP182220720	18222	218	720	6/26/09 6:27	36.6481	-119.7759	34.3
ALPSRP182220730	18222	218	730	6/26/09 6:27	37.1426	-119.8842	34.3
ALPSRP195640690	19564	218	690	9/26/09 6:27	35.16	-119.4506	34.3
ALPSRP195640700	19564	218	700	9/26/09 6:28	35.6551	-119.5569	34.3
ALPSRP195640710	19564	218	710	9/26/09 6:28	36.1495	-119.6636	34.3
ALPSRP195640720	19564	218	720	9/26/09 6:28	36.6443	-119.771	34.3
ALPSRP195640730	19564	218	730	9/26/09 6:28	37.1386	-119.8799	34.3
ALPSRP209060690	20906	218	690	12/27/09 6:27	35.156	-119.4426	34.3
ALPSRP209060700	20906	218	700	12/27/09 6:28	35.6508	-119.5485	34.3
ALPSRP209060710	20906	218	710	12/27/09 6:28	36.1453	-119.6565	34.3
ALPSRP209060720	20906	218	720	12/27/09 6:28	36.6399	-119.7648	34.3
ALPSRP209060730	20906	218	730	12/27/09 6:28	37.1343	-119.8725	34.3
ALPSRP222480690	22248	218	690	3/29/10 6:27	35.1356	-119.4289	34.3
ALPSRP222480700	22248	218	700	3/29/10 6:27	35.6301	-119.5359	34.3
ALPSRP222480710	22248	218	710	3/29/10 6:27	36.1248	-119.6435	34.3
ALPSRP222480720	22248	218	720	3/29/10 6:27	36.6193	-119.7505	34.3
ALPSRP222480730	22248	218	730	3/29/10 6:28	37.114	-119.8576	34.3
ALPSRP229190690	22919	218	690	5/14/10 6:27	35.1595	-119.4351	34.3
ALPSRP229190700	22919	218	700	5/14/10 6:27	35.6543	-119.541	34.3
ALPSRP229190710	22919	218	710	5/14/10 6:27	36.149	-119.6471	34.3
ALPSRP229190720	22919	218	720	5/14/10 6:27	36.6436	-119.7539	34.3
ALPSRP229190730	22919	218	730	5/14/10 6:27	37.1381	-119.8614	34.3
ALPSRP235900690	23590	218	690	6/29/10 6:26	35.1623	-119.4335	34.3
ALPSRP235900700	23590	218	700	6/29/10 6:26	35.6571	-119.5404	34.3
ALPSRP235900710	23590	218	710	6/29/10 6:26	36.1516	-119.6464	34.3
ALPSRP235900720	23590	218	720	6/29/10 6:27	36.6463	-119.7535	34.3
ALPSRP235900730	23590	218	730	6/29/10 6:27	37.1408	-119.8605	34.3
ALPSRP262740690	26274	218	690	12/30/10 6:23	35.1628	-119.4223	34.3
ALPSRP262740700	26274	218	700	12/30/10 6:24	35.658	-119.5281	34.3
ALPSRP262740710	26274	218	710	12/30/10 6:24	36.1525	-119.6341	34.3
ALPSRP262740720	26274	218	720	12/30/10 6:24	36.6471	-119.7404	34.3
ALPSRP262740730	26274	218	730	12/30/10 6:24	37.1419	-119.8478	34.3
San Joaquin Valley, Center swath							
ALPSRP077340710	7734	219	710	7/8/07 6:28	36.1438	-120.1903	34.3
ALPSRP077340720	7734	219	720	7/8/07 6:28	36.6383	-120.2975	34.3
ALPSRP077340730	7734	219	730	7/8/07 6:28	37.1326	-120.4049	34.3
ALPSRP084050710	8405	219	710	8/23/07 6:28	36.1498	-120.1903	34.3
ALPSRP084050720	8405	219	720	8/23/07 6:28	36.6442	-120.2972	34.3
ALPSRP084050730	8405	219	730	8/23/07 6:28	37.139	-120.4046	34.3
ALPSRP097470710	9747	219	710	11/23/07 6:27	36.1511	-120.1839	34.3

ALPSRP097470720	9747	219	720	11/23/07 6:28	36.6456	-120.2909	34.3
ALPSRP097470730	9747	219	730	11/23/07 6:28	37.1396	-120.3999	34.3
ALPSRP104180710	10418	219	710	1/8/08 6:27	36.1413	-120.181	34.3
ALPSRP104180720	10418	219	720	1/8/08 6:27	36.6361	-120.2879	34.3
ALPSRP104180730	10418	219	730	1/8/08 6:27	37.1306	-120.3949	34.3
ALPSRP110890710	11089	219	710	2/23/08 6:26	36.151	-120.1721	34.3
ALPSRP110890720	11089	219	720	2/23/08 6:27	36.6458	-120.2785	34.3
ALPSRP110890730	11089	219	730	2/23/08 6:27	37.1406	-120.3872	34.3
ALPSRP117600710	11760	219	710	4/9/08 6:26	36.1285	-120.1621	34.3
ALPSRP117600720	11760	219	720	4/9/08 6:26	36.6231	-120.2689	34.3
ALPSRP117600730	11760	219	730	4/9/08 6:26	37.1177	-120.3762	34.3
ALPSRP124310710	12431	219	710	5/25/08 6:25	36.1481	-120.1694	34.3
ALPSRP124310720	12431	219	720	5/25/08 6:25	36.6425	-120.2761	34.3
ALPSRP124310730	12431	219	730	5/25/08 6:25	37.1371	-120.3834	34.3
ALPSRP131020710	13102	219	710	7/10/08 6:25	36.1508	-120.2045	34.3
ALPSRP131020720	13102	219	720	7/10/08 6:25	36.6451	-120.3129	34.3
ALPSRP131020730	13102	219	730	7/10/08 6:25	37.1393	-120.422	34.3
ALPSRP164570710	16457	219	710	2/25/09 6:28	36.1436	-120.2129	34.3
ALPSRP164570720	16457	219	720	2/25/09 6:29	36.6382	-120.3202	34.3
ALPSRP164570730	16457	219	730	2/25/09 6:29	37.1326	-120.4297	34.3
ALPSRP171280710	17128	219	710	4/12/09 6:29	36.1441	-120.2029	34.3
ALPSRP171280720	17128	219	720	4/12/09 6:29	36.6389	-120.3098	34.3
ALPSRP171280730	17128	219	730	4/12/09 6:29	37.1331	-120.4194	34.3
ALPSRP198120710	19812	219	710	10/13/09 6:30	36.1382	-120.1937	34.3
ALPSRP198120720	19812	219	720	10/13/09 6:30	36.6325	-120.3021	34.3
ALPSRP198120730	19812	219	730	10/13/09 6:30	37.1266	-120.4124	34.3
ALPSRP211540710	21154	219	710	1/13/10 6:30	36.1448	-120.1908	34.3
ALPSRP211540720	21154	219	720	1/13/10 6:30	36.6396	-120.2979	34.3
ALPSRP211540730	21154	219	730	1/13/10 6:30	37.1338	-120.407	34.3
ALPSRP224960710	22496	219	710	4/15/10 6:29	36.1538	-120.1853	34.3
ALPSRP224960720	22496	219	720	4/15/10 6:29	36.6482	-120.2922	34.3
ALPSRP224960730	22496	219	730	4/15/10 6:30	37.1431	-120.3994	34.3
ALPSRP231670710	23167	219	710	5/31/10 6:29	36.1432	-120.1807	34.3
ALPSRP231670720	23167	219	720	5/31/10 6:29	36.6381	-120.2874	34.3
ALPSRP231670730	23167	219	730	5/31/10 6:29	37.1326	-120.3944	34.3
ALPSRP258510710	25851	219	710	12/1/10 6:26	36.1273	-120.169	34.3
ALPSRP258510720	25851	219	720	12/1/10 6:27	36.6221	-120.2754	34.3
ALPSRP258510730	25851	219	730	12/1/10 6:27	37.1165	-120.3836	34.3
Southern Sacramento Valley							
ALPSRP048750760	4875	221	760	12/24/06 6:33	38.6236	-121.8327	34.3
ALPSRP048750770	4875	221	770	12/24/06 6:33	39.1176	-121.9427	34.3
ALPSRP048750780	4875	221	780	12/24/06 6:33	39.6116	-122.0537	34.3
ALPSRP048750790	4875	221	790	12/24/06 6:33	40.1057	-122.1647	34.3
ALPSRP062170760	6217	221	760	3/26/07 6:33	38.6226	-121.8129	34.3
ALPSRP062170770	6217	221	770	3/26/07 6:33	39.1168	-121.923	34.3
ALPSRP062170780	6217	221	780	3/26/07 6:33	39.6111	-122.0337	34.3
ALPSRP062170790	6217	221	790	3/26/07 6:34	40.1052	-122.1447	34.3
ALPSRP089010760	8901	221	760	9/26/07 6:33	38.6206	-121.8074	34.3
ALPSRP089010770	8901	221	770	9/26/07 6:33	39.1146	-121.9187	34.3
ALPSRP089010780	8901	221	780	9/26/07 6:33	39.6085	-122.0291	34.3
ALPSRP089010790	8901	221	790	9/26/07 6:33	40.1027	-122.1402	34.3

ALPSRP102430760	10243	221	760	12/27/07 6:32	38.6228	-121.803	34.3
ALPSRP102430770	10243	221	770	12/27/07 6:32	39.1171	-121.9127	34.3
ALPSRP102430780	10243	221	780	12/27/07 6:32	39.6111	-122.0227	34.3
ALPSRP102430790	10243	221	790	12/27/07 6:33	40.1051	-122.1339	34.3
ALPSRP109140760	10914	221	760	2/11/08 6:32	38.6216	-121.7892	34.3
ALPSRP115850760	11585	221	760	3/28/08 6:31	38.6229	-121.7873	34.3
ALPSRP115850770	11585	221	770	3/28/08 6:31	39.1171	-121.8964	34.3
ALPSRP115850780	11585	221	780	3/28/08 6:31	39.6111	-122.0067	34.3
ALPSRP115850790	11585	221	790	3/28/08 6:31	40.1052	-122.1172	34.3
ALPSRP122560760	12256	221	760	5/13/08 6:30	38.3944	-121.7402	34.3
ALPSRP122560770	12256	221	770	5/13/08 6:30	38.8894	-121.8487	34.3
ALPSRP122560780	12256	221	780	5/13/08 6:30	39.3851	-121.9588	34.3
ALPSRP122560790	12256	221	790	5/13/08 6:31	39.8814	-122.072	34.3
ALPSRP149400760	14940	221	760	11/13/08 6:32	38.6226	-121.8397	34.3
ALPSRP149400770	14940	221	770	11/13/08 6:32	39.1165	-121.9501	34.3
ALPSRP149400780	14940	221	780	11/13/08 6:32	39.6107	-122.0615	34.3
ALPSRP149400790	14940	221	790	11/13/08 6:32	40.1047	-122.1732	34.3
ALPSRP156110760	15611	221	760	12/29/08 6:33	38.6233	-121.8382	34.3
ALPSRP156110770	15611	221	770	12/29/08 6:33	39.1176	-121.9487	34.3
ALPSRP156110780	15611	221	780	12/29/08 6:33	39.6106	-122.0622	34.3
ALPSRP156110790	15611	221	790	12/29/08 6:33	40.1046	-122.1744	34.3
ALPSRP169530760	16953	221	760	3/31/09 6:34	38.6096	-121.8247	34.3
ALPSRP182950760	18295	221	760	7/1/09 6:34	38.6195	-121.8251	34.3
ALPSRP182950770	18295	221	770	7/1/09 6:35	39.1136	-121.9352	34.3
ALPSRP182950780	18295	221	780	7/1/09 6:35	39.6076	-122.0459	34.3
ALPSRP182950790	18295	221	790	7/1/09 6:35	40.1017	-122.1577	34.3
ALPSRP196370760	19637	221	760	10/1/09 6:35	38.6246	-121.8177	34.3
ALPSRP196370770	19637	221	770	10/1/09 6:35	39.1186	-121.9279	34.3
ALPSRP196370780	19637	221	780	10/1/09 6:35	39.6126	-122.0387	34.3
ALPSRP196370790	19637	221	790	10/1/09 6:35	40.1067	-122.1497	34.3
ALPSRP209790760	20979	221	760	1/1/10 6:35	38.6206	-121.8099	34.3
ALPSRP209790770	20979	221	770	1/1/10 6:35	39.1148	-121.92	34.3
ALPSRP209790780	20979	221	780	1/1/10 6:35	39.6091	-122.0307	34.3
ALPSRP209790790	20979	221	790	1/1/10 6:35	40.1032	-122.1417	34.3
ALPSRP229920760	22992	221	760	5/19/10 6:34	38.6068	-121.7945	34.3
ALPSRP229920770	22992	221	770	5/19/10 6:34	39.1011	-121.9042	34.3
ALPSRP229920780	22992	221	780	5/19/10 6:34	39.5951	-122.0159	34.3
ALPSRP229920790	22992	221	790	5/19/10 6:34	40.0892	-122.1282	34.3
ALPSRP236630760	23663	221	760	7/4/10 6:33	38.6218	-121.796	34.3
ALPSRP236630770	23663	221	770	7/4/10 6:34	39.1161	-121.9054	34.3
ALPSRP236630780	23663	221	780	7/4/10 6:34	39.6101	-122.0157	34.3
ALPSRP236630790	23663	221	790	7/4/10 6:34	40.1042	-122.1267	34.3
ALPSRP243340780	24334	221	780	8/19/10 6:33	39.6121	-122.0147	34.3
ALPSRP243340790	24334	221	790	8/19/10 6:33	40.1061	-122.1259	34.3
ALPSRP256760760	25676	221	760	11/19/10 6:32	38.6221	-121.7922	34.3
ALPSRP256760770	25676	221	770	11/19/10 6:32	39.1164	-121.9018	34.3
ALPSRP256760780	25676	221	780	11/19/10 6:32	39.6109	-122.0123	34.3
ALPSRP256760790	25676	221	790	11/19/10 6:32	40.1048	-122.123	34.3

Radarsat-2 Data Listing

The Radarsat-2 satellite (Table 1) provided the more recent satellite data used for this report. Radarsat-2 is the second radar satellite launched by the Canadian Space Agency. It is in a polar orbit which allows it to view any point on the globe every 24 days (its minimum repeat period for subsidence detection). It uses a wavelength of about 2", which makes it more sensitive than longer-wavelength radar systems to disturbances of the ground that can spoil the phase information. Spatial resolution is typically around 50-100 feet, but during InSAR processing, we usually average to about 300' to decrease noise.

For this study, we purchased Radarsat-2 data for 2 orbital tracks, covering most of the San Joaquin Valley and the southern part of the Sacramento Valley (Fig. A1). Tracks are cut up into frames; 2 frames were acquired for the eastern track covering the eastern part of the San Joaquin Valley and 1 frame was acquired for the western track covering the western side of the San Joaquin Valley, with an additional frame on the same track covering the southern part of the Sacramento Valley. Dates and frame ID numbers are listed below.

By working with the Canadian Space Agency, we acquired 6 dates of coverage for the eastern track and 9 dates for the western track . For the eastern track, we obtained coverage on 3 May 2014, 27 May 2014, 18 October 2014, 11 November 2014, 5 December 2014, and 22 January 2015. The gap between May and October was caused by a miscommunication so that satellite acquisition was stopped during that time. The southern boundary of the eastern track was determined due to the competing data acquisitions in a different data mode by oil companies monitoring subsidence in the oil fields west of Bakersfield. For the western track, including the west side of the San Joaquin Valley and the southern part of the Sacramento Valley, we obtained SAR coverage from 20 May 2014 to 28 November 2014.

As we processed the data for the eastern track, we realized that the 5 December 2014 acquisition had problems with the data. Missing lines were detected and the interferograms associated with that date are distinctly different from other interferometric pairs. For this reason, we excluded that date from our processing and present results from the remaining 5 dates from that track. The subsidence map derived from the western track for the San Joaquin Valley showed the same subsidence features as the eastern track, so we used it as a validation for the eastern result, but don't show the map here.

A detailed listing of all Radarsat-2 data used for this report is given in Table A2 below. Orbits are all ascending (SE – NW), Beam mode is Fine resolution, Wide-swath mode. Polarization is HH. Data were purchased from MDA Geospatial Services Inc. through Resource Strategies Inc.

Table A2. Listing of all Radarsat-2 data used in this report.

Date	Time	Orbit	Abs. Orbit	Beam	Pol.	Angle	Center Lat/Lon
San Joaquin Valley- East							
5/3/14	1:57:27	96-157A	33321.1	F0W2	HH	31.27	36°34'N/119°56'W
5/3/14	1:57:48	96-157A	33321.11	F0W2	HH	31.27	37°48'N/120°13'W
5/27/14	1:57:26	97-157A	33664.1	F0W2	HH	31.27	36°34'N/119°56'W
5/27/14	1:57:47	97-157A	33664.11	F0W2	HH	31.27	37°48'N/120°13'W
10/18/14	1:56:47	103-157A	35722.1	F0W2	HH	31.27	36°35'N/119°56'W
10/18/14	1:57:08	103-157A	35722.1	F0W2	HH	31.27	37°49'N/120°13'W
11/11/14	1:56:47	104-157A	36065.1	F0W2	HH	31.27	36°35'N/119°56'W
11/11/14	1:57:08	104-157A	36065.1	F0W2	HH	31.27	37°49'N/120°13'W
12/5/14	1:56:47	105-157A	36408.1	F0W2	HH	31.27	36°35'N/119°56'W
12/5/14	1:57:08	105-157A	36408.1	F0W2	HH	31.27	37°49'N/120°13'W
1/22/15	1:57:20		37094	F0W2	HH	31.27	36°36'N/119°56'W
1/22/15	1:57:40		37094	F0W2	HH	31.27	37°48'N/120°13'W
Sacramento Valley							
5/20/14	2:02:18	97-57A	33564.11	F0W2	HH	31.27	38°53'N/121°31'W
6/13/14	2:02:17	98-57A	33907.11	F0W2	HH	31.27	38°53'N/121°31'W
7/7/14	2:02:16	99-57A	34250.11	F0W2	HH	31.27	38°53'N/121°31'W
7/31/14	2:02:16	100-57A	34593.11	F0W2	HH	31.27	38°53'N/121°31'W
8/24/14	2:02:17	101-57A	34936.11	F0W2	HH	31.27	38°53'N/121°31'W
9/17/14	2:02:17	102-57A	35279.11	F0W2	HH	31.27	38°52'N/121°31'W
10/11/14	2:01:39	103-57A	35622.1	F0W2	HH	31.27	38°56'N/121°32'W
11/4/14	2:01:39	104-57A	35965.1	F0W2	HH	31.27	38°56'N/121°32'W
11/28/14	2:01:39	105-57A	36308.1	F0W2	HH	31.27	38°56'N/121°32'W
San Joaquin Valley- West							
5/20/14	2:01:43	97-57A	33564.11	F0W2	HH	31.27	36°50'N/121°02'W
6/13/14	2:01:42	98-57A	33907.11	F0W2	HH	31.27	36°50'N/121°02'W
7/7/14	2:01:42	99-57A	34250.1	F0W2	HH	31.27	36°50'N/121°02'W
7/31/14	2:01:42	100-57A	34593.1	F0W2	HH	31.27	36°50'N/121°02'W
8/24/14	2:01:42	101-57A	34936.11	F0W2	HH	31.27	36°50'N/121°03'W
9/17/14	2:01:42	102-57A	35279.11	F0W2	HH	31.27	36°50'N/121°03'W
10/11/14	2:01:41	103-57A	35622.1	F0W2	HH	31.27	36°50'N/121°03'W
11/4/14	2:01:41	104-57A	35965.1	F0W2	HH	31.27	36°50'N/121°03'W
11/28/14	2:01:39	105-57A	36308.1	F0W2	HH	31.27	36°50'N/121°03'W

UAVSAR

The two UAVSAR flight lines used for evaluating subsidence of the California Aqueduct were line ID CValle_13300 (southern section) and line ID Snjoaq_14511 (northern section). Table A3 shows the flight dates, UAVSAR flight IDs, and temporal baselines for lines 13300 and 14511. Each acquisition was used in at least three interferograms to provide sufficient redundancy to eliminate systematic effects from atmospheric variation and aircraft motion artifacts. Acquisition of line 14511 began earliest, in July 2013, and extended through

March 2015. We were able to use 1-year temporal baseline, same-season interferograms with this data set, increasing the accuracy of small-scale cumulative subsidence measurements. Acquisition of line 13300 began in April 2014 and extended through January 2015, so we were not able to include the season-to-season interferograms in that analysis. Further information about UAVSAR can be found at http://uavsar.jpl.nasa.gov.

Table A3. UAVSAR line ID, flight ID, and acquisition date of the data used for evaluating subsidence of the California Aqueduct during the 2014 drought.

UAVSAR Line ID 14511			UAVSAR Line ID 13300		
Acq. No.	**Flight ID**	**Date of acquisition**	**Acq. No.**	**Flight ID**	**Date of acquisition**
1	13129	7/19/2013	1	14033	4/2/2014
2	13165	10/31/2013	2	14062	5/15/2014
3	14005	1/17/2014	3	14086	6/16/2014
4	14019	2/12/2014	4	14112	8/14/2014
5	14033	4/2/2014	5	14140	10/6/2014
6	14068	5/29/2014	6	14166	11/13/2014
7	14086	6/16/2014	7	15002	1/7/2015
8	14112	8/14/2014			
9	14140	10/6/2014			
10	14166	11/13/2014			
11	15002	1/7/2015			
12	15017	3/10/2015			

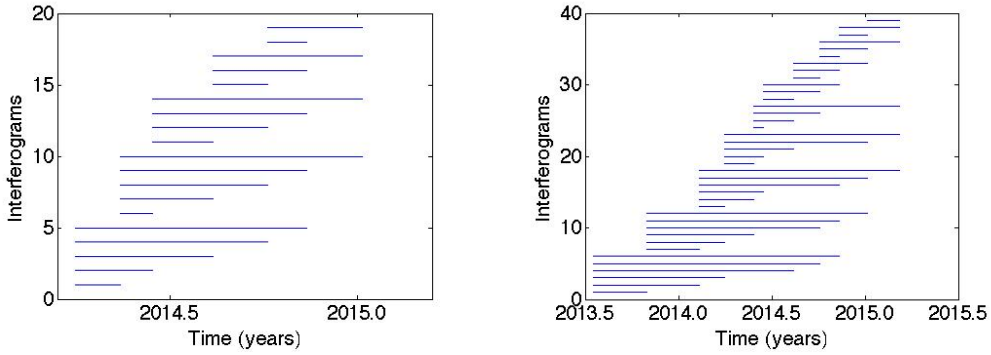

Figure A2. Graph showing the pairs of images used to form interferograms used for UAVSAR line ID 13300 (left) and line ID 14511 (right). In the plot, the bar extends from the date of acquisition 1 to the date of acquisition 2.

UAVSAR uncertainties

Figures A3 and A4 show the uncertainties associated with the vertical displacement (subsidence/uplift) measurements. These uncertainties cover random errors, but do not include systematic errors, i.e., systematic shifts that affect all interferograms, for example, persistent water vapor within mountain valleys, were it present in all images, would not be included in the error estimation.

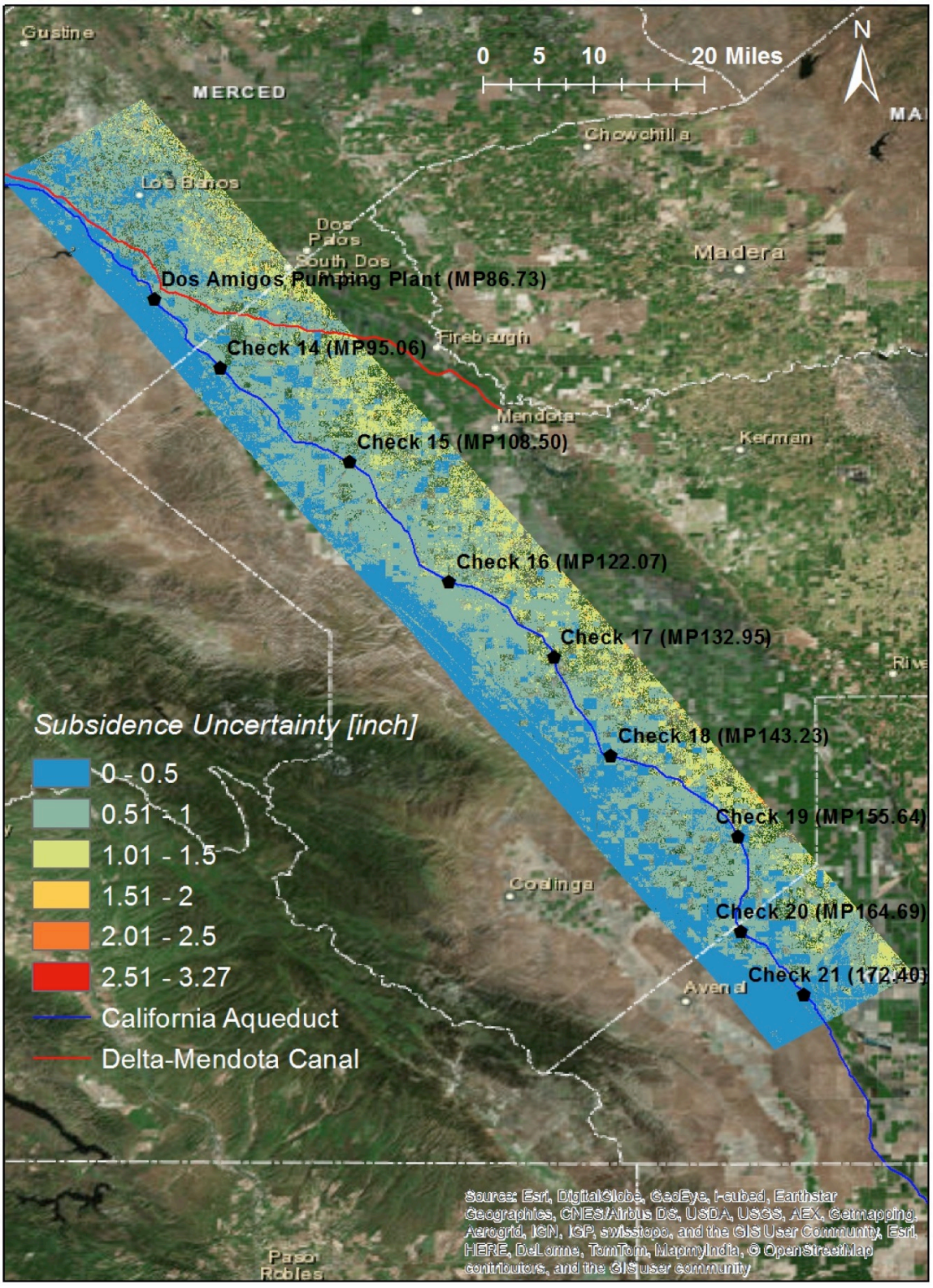

Figure A3. Uncertainty in the vertical movement derived from UAVSAR line ID 14511, covering the northern section of the California Aqueduct within the area overseen by the San Luis Field Division.

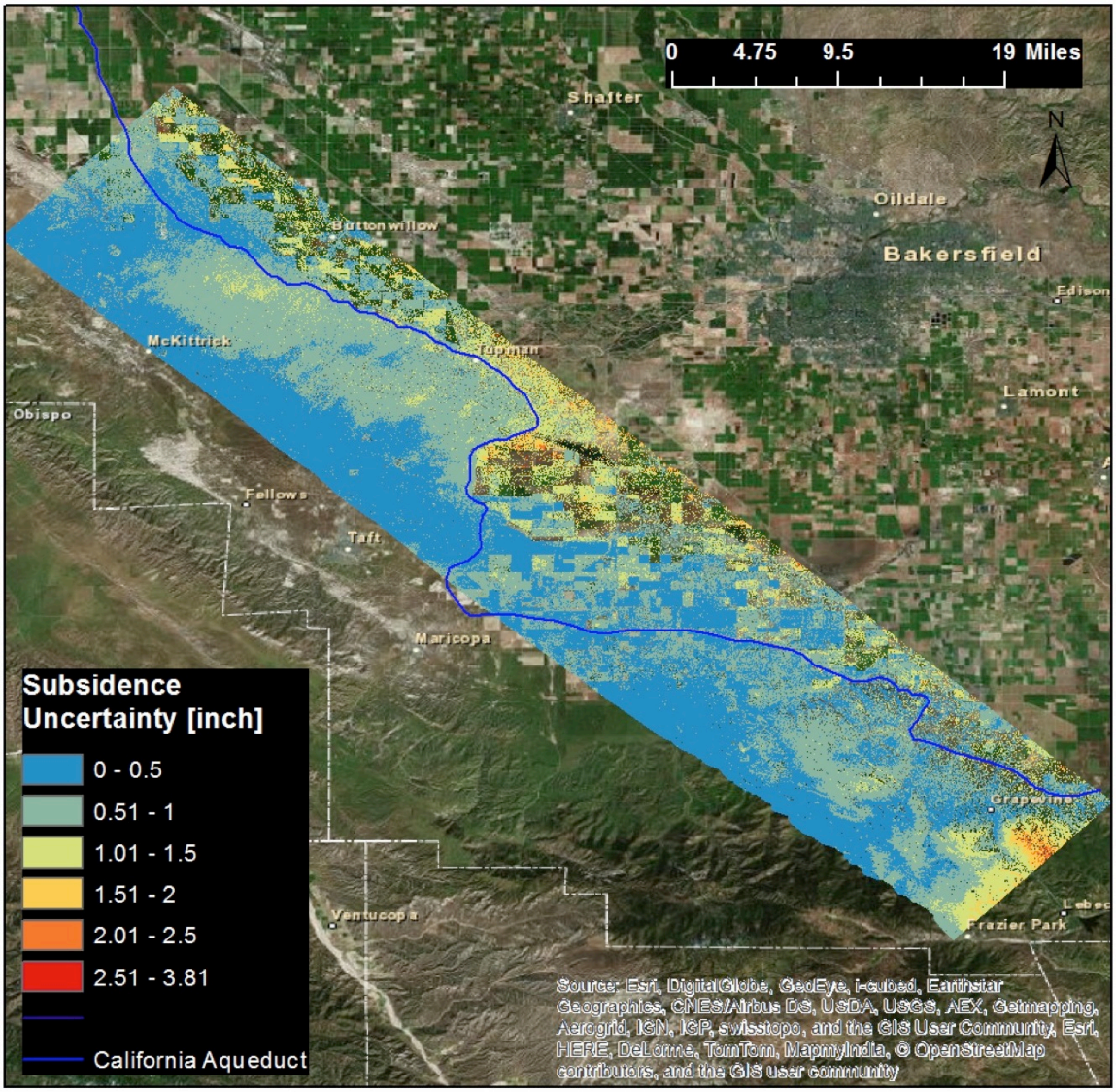

Figure A4. Uncertainty in the subsidence derived from UAVSAR line ID 13300, covering the southern section of the California Aqueduct within the area overseen by the San Joaquin Field Division.